



## Short communication

## Longitudinal aerodynamic modeling and verification for air-launch-to-orbit system during stage separation

Lei Yang<sup>a,b,\*</sup>, Zhengyin Ye<sup>d</sup>, Wenhao Li<sup>a,b</sup>, Quanhua Sun<sup>a,c</sup><sup>a</sup> Laboratory for Aerospace Science and Technology, Institute of Mechanics, Chinese Academy of Sciences, Beijing 100190, PR China<sup>b</sup> Key Lab of Mechanics in Advanced Manufacturing, Institute of Mechanics, Chinese Academy of Sciences, Beijing 100190, PR China<sup>c</sup> State Key Laboratory of High-Temperature Gas Dynamics, Institute of Mechanics, Chinese Academy of Sciences, Beijing 100190, PR China<sup>d</sup> National Key Laboratory on Aerodynamic Design and Research, School of Aeronautics, Northwestern Polytechnical University, Xi'an 710072, PR China

## ARTICLE INFO

## Article history:

Received 27 January 2021

Received in revised form 20 June 2021

Accepted 21 June 2021

Available online 30 June 2021

Communicated by Qiulin Qu

## Keywords:

Store separation

Aerodynamic modeling

Interference aerodynamics

Dynamic simulation

Air-launch-to-orbit

## ABSTRACT

The stage separation is one of key issues for air-launch-to-orbit system. In this process, the elastic deformation of carrier causes periodic pulsation in interference aerodynamics and may lead to modal coupling and dynamics instability of spacecraft. The dynamic responses and stability of the two vehicles should be considered carefully. The CFD-based dynamic simulation method has high accuracy but requires large computation cost. In this study, a new reduced-order modeling method is developed, which is for unsteady aerodynamics of the air-launch-to-orbit system with considering the elastic deformations of carrier. Based on the physical mechanism of interference aerodynamics factors, the model input parameters are decoupled and the modeling difficulty is reduced. By coupling the unsteady aerodynamic model, structural dynamics equations and rigid body dynamic equations, the longitudinal dynamic responses of air-launch-to-orbit system during stage separation are simulated. Through comparison, those results have good agreement with traditional CFD-based method, and the simulation efficiency of new method is improved greatly. The new modeling method is applicable to the air-launch-to-orbit system and can provide guidance for similar engineering issues.

© 2021 Elsevier Masson SAS. All rights reserved.

## 1. Introduction

Air-launch-to-orbit is the system that has stores carried aloft and launched the store from the carrier aircraft to the orbit. Usually, the stores are launch vehicles, aerospace planes or other spacecraft. Compared to the traditional ground launch, the air launch has the characteristics of higher flexibility and lower cost [1,2].

The stage separation is one of the key issues for air-launch-to-orbit system [3]. In this period, the relative position and posture of carrier and the spacecraft show dynamic changes [4–6], and there will be strong aerodynamic interference between the two vehicles [7,8]. Normally, the carrier is a large transport aircraft such as WhiteKnight Two and Stratolaunch, which has a relatively smaller structure mass factor for larger load factor and longer voyage. Then, there will be elastic deformation during flight. At the moment of separation, there is a sudden change in the normal overload of carrier, which will act as an excitation to generate elastic vibrations in the wings, and then causes the periodic interference aerodynamics. When the interference aerodynamic modal frequency is close to that of the longitudinal short-period modal frequency of the spacecraft, it may lead to modal coupling and dynamics instability of the spacecraft. Therefore, the unsteady aeroelastic characteristics of carrier must be considered in the beginning of stage separation maneuver. To sum up, the separation process of air-launch-to-orbit system is a multidisciplinary dynamics problem that couples the unsteady aerodynamics, structural dynamics, and flight dynamics, the interference aerodynamics and dynamic characteristics of the vehicles needs to be carefully studied.

Wind tunnel test can measure the aerodynamic forces and dynamic responses of air-launch-to-orbit system during separation reliably [9,10]. However, it has high requirements for the installation and positioning accuracy of experimental equipment, and the experimental cost is higher. Since the 1970s, with the rapid development of computer technology, the CFD method has made considerable progress. In

\* Corresponding author at: Laboratory for Aerospace Science and Technology, Institute of Mechanics, Chinese Academy of Sciences, Beijing 100190, PR China.

E-mail address: yanglei@imech.ac.cn (L. Yang).

the early 1990s, the development and verification of CFD-based multi-body separation simulation programs have attracted the attention of researchers. In 1991, the separation experiment of a wing-pylon-finned body was carried out by Air Force Wright Laboratory (AFWL) and Arnold Engineering Development Center (AEDC) [11]. This experiment provided a benchmark example for the multi-body separation simulation program to verify the reliability of the code. In 1992, the store separation process of wing-pylon-finned body was simulated with CFD-based method by AFWL. The simulation results agreed well with the experiment [12]. Subsequently, the simulation method was quickly extended to engineering problems, and applied to air launch platforms such as F/A-18 [13], F-15E [14,15], F-16 [16], B-52 [17], and so on.

After more than 30 years of development, it is mature for CFD-based method to solve the multi-body separation problems. However, few investigations take attention on the elastic deformation of the aircraft during separation process. In our previous research, by coupling Navier-Stokes equations, structure dynamic equations and rigid body equations, the stage separation problem with considering the elastic deformation of carrier was researched [7,8]. However, the computational cost of numerical method is very large and it is unacceptable for engineering problems. During the simulation, more than 99% of the calculated amount is generated from the mesh deformation and the solution of N-S equation. The CFD solver is called frequently due to the physical time step is based on the highest frequency of the structural mode. Therefore, a simple and efficient solution method for obtaining the dynamic response of the aircrafts is required and an accurate and efficient aerodynamic solver is needed.

It is suitable for reduced-order model (ROM) to replace the CFD solver for dynamic simulation. The calculation cost of ROM is reflected in the sample calculation. Once the model is established, a large number of simulations for different operating conditions can be carried out with few computational expense. In recent years, the reduced-order model has a wide range of applications, such as time domain dynamic analysis [18,19], aeroelastic global structural optimization [20], complex flow analysis [21], convergence acceleration of solver [22], aerodynamic shape optimization [23,24], nonlinear dynamic structure modeling [25], and so on.

In this study, a new CFD-based reduced-order modeling method for unsteady aerodynamics of air-launch-to-orbit system during stage separation are developed. In aerodynamic modeling, the elastic deformations of the carrier are considered. Based on the physical mechanism of interference aerodynamics factors, the model input parameters are decoupled and the modeling difficulty is reduced. Employing the input and output data calculated by the CFD-based multidisciplinary simulation method, the parameters of aerodynamic model are identified. Through coupling the unsteady aerodynamic model, structural dynamics equations and rigid body dynamic equations, the longitudinal dynamic responses of air-launch-to-orbit system during stage separation are simulated. By comparing those results with that of CFD/CSD/RBD method, the practicability, accuracy and efficiency of the modeling method developed in this paper are verified.

## 2. Unsteady aerodynamic modeling method

### 2.1. The kinetic model of air-launch-to-orbit system during separation process

The longitudinal kinetic model of air-launch-to-orbit system during separation is established in this section. First of all, the physical assumptions involved in the model are explained as follows:

1. Assuming that the carrier is an elastomer, and the elastic deformations of carrier during flight are considered.
2. Assuming that the carrier remains straight line flight at constant altitude during separation.
3. Assuming that the spacecraft is a rigid body with no elastic deformation, and only longitudinal pitching and plunging dynamic motions are considered.
4. The interference aerodynamics of spacecraft caused by the carrier are considered in the kinetic model. The interference aerodynamics of the carrier caused by the spacecraft are ignored.

For the fourth assumption, the physics interpretation is as follows. Firstly, compared with the carrier, the size and weight of spacecraft is smaller. The interference aerodynamics caused by spacecraft is relatively smaller compared with aerodynamic load of carrier. Secondly, the relative distance between the two vehicles keeps increasing during stage separation, and the interference aerodynamics is reducing.

Dynamic equation of elastic aircraft can be expressed as:

$$\begin{cases} m \frac{d\mathbf{V}}{dt} = \mathbf{F}_r \\ \frac{d\mathbf{h}}{dt} = \mathbf{M}_r \\ \mathbf{M}\ddot{\boldsymbol{\xi}} + \mathbf{G}\dot{\boldsymbol{\xi}} + \mathbf{K}\boldsymbol{\xi} = \mathbf{F} \end{cases} \quad (1)$$

where,  $\mathbf{F}_r$  and  $\mathbf{M}_r$  represent resultant force and moment vector respectively;  $\mathbf{V}$  means the velocity vector;  $\mathbf{h}$  denotes moment of momentum;  $\boldsymbol{\xi}$  is the generalized displacement,  $\mathbf{M}$  is the generalized mass matrix;  $\mathbf{G}$  is the generalized structural damping matrix;  $\mathbf{K}$  is the generalized stiffness matrix; and  $\mathbf{F}$  is the generalized force.

By assumption 1 and 2,  $d\mathbf{V}/dt$  and  $d\mathbf{h}/dt$  of carrier are zero during separation process. The dynamic equation can be expressed as:

$$\mathbf{M}\ddot{\boldsymbol{\xi}} + \mathbf{G}\dot{\boldsymbol{\xi}} + \mathbf{K}\boldsymbol{\xi} = \mathbf{F} \quad (2)$$

By assumption 3, the dynamic equation of spacecraft can be expressed as:

$$\begin{cases} m\ddot{z} = F_z - mg \cos \theta \\ I_y \dot{q} = M_y \end{cases} \quad (3)$$

where,  $\ddot{z}$  is normal acceleration;  $m$  means the mass of spacecraft;  $F_z$  denotes normal force;  $q$  and  $\theta$  are pitching angle velocity and pitching angle respectively;  $I_y$  represents the principal moments of inertia along the y axis;  $M_y$  refers to the pitching moment.

Then, the longitudinal kinetic model of air-launch-to-orbit system during separation can be expressed as:

$$\begin{cases} \mathbf{M}\ddot{\xi} + \mathbf{G}\dot{\xi} + \mathbf{K}\xi = \mathbf{F} \\ m\ddot{z} = F_z - mg \cos \theta \\ I_y \dot{q} = M_y \end{cases} \quad (4)$$

## 2.2. The unsteady aerodynamic modeling method of the carrier

In general, when an aircraft (not included the flexible aircraft) is in the normal flight conditions, the elastic deformation of the aircraft satisfies the small deformation hypothesis. The linearized model can be used to describe the generalized aerodynamic force of carrier.

In this study, the autoregressive with exogenous input (ARX) model is employed. For the MIMO system (Multiple input multiple output system), the ARX model is given as follows [26]:

$$\mathbf{y}(k) = \sum_{i=1}^{na} \mathbf{A}_i \mathbf{y}(k-i) + \sum_{i=0}^{nb-1} \mathbf{B}_i \mathbf{u}(k-i) \quad (5)$$

where,  $\mathbf{u}$  and  $\mathbf{y}$  are input and output vectors of the model;  $na$  and  $nb$  mean the delay order of the input and feedback of the model respectively;  $\mathbf{A}_i$  and  $\mathbf{B}_i$  represent matrices of constant coefficients to be estimated. For carrier, the model input and output are its generalized displacement and generalized aerodynamic force, respectively. The state space model of ARX in continuous form can be expressed as follows:

$$\begin{cases} \dot{\mathbf{x}}_a(t) = \mathbf{A}_a \mathbf{x}_a(t) + \mathbf{B}_a \mathbf{x}_b(t) \\ \mathbf{f}_a(t) = \mathbf{C}_a \mathbf{x}_a(t) + \mathbf{D}_a \mathbf{x}_b(t) + \mathbf{f}_{a0} \end{cases} \quad (6)$$

where, the state vector  $\mathbf{x}_a = [\mathbf{f}_a(k-1), \dots, \mathbf{f}_a(k-na), \xi(k-1), \dots, \xi(k-nb+1)]^T$ ,  $\mathbf{x}_b = [\xi(k)]^T$ , and  $\xi$  is generalized displacement;  $\mathbf{f}_a$  is the modal aerodynamic coefficient matrix;  $\mathbf{f}_{a0}$  is the static aerodynamic coefficient matrix;  $\mathbf{A}_a$ ,  $\mathbf{B}_a$ ,  $\mathbf{C}_a$  and  $\mathbf{D}_a$  are matrices of constant coefficients to be estimated.

## 2.3. The aerodynamic modeling method of spacecraft

During separation, the aerodynamic forces of spacecraft are influenced by the following factors: 1. The aerodynamic configurations and flight attitude; 2. The relative distance between carrier and spacecraft; 3. The elastic deformation of the carrier. Thus, the aerodynamic models of spacecraft are expressed as:

$$\begin{aligned} F_z(\alpha, \theta, \dot{\theta}, \xi, \dot{\xi}, \ddot{\xi}, c, t) &= F_{z1}(\alpha, \theta, \dot{\theta}) + F_{z2}(\xi, c) + F_{z3}(\xi, \dot{\xi}, \ddot{\xi}, c, t) \\ M_y(\alpha, \theta, \dot{\theta}, \xi, \dot{\xi}, \ddot{\xi}, c, t) &= M_{y1}(\alpha, \theta, \dot{\theta}) + M_{y2}(\xi, c) + M_{y3}(\xi, \dot{\xi}, \ddot{\xi}, c, t) \end{aligned} \quad (7)$$

where,  $F_1$  is the aerodynamic forces caused by the aerodynamic configurations and flight attitude and is the function of angle of attack  $\alpha$ , pitching angle  $\theta$  and pitching rate  $\dot{\theta}$ .  $F_2$  is the interaction aerodynamic forces caused by elastic carrier and is functions of the relative distance  $c$  and the static elastic deformation  $\xi$  of the carrier.  $F_3$  is the interaction aerodynamics increment caused by the dynamic elastic deformation of carrier and is function of  $\xi$ ,  $\dot{\xi}$ ,  $\ddot{\xi}$ ,  $c$  and time  $t$ .  $\xi$ ,  $\dot{\xi}$  and  $\ddot{\xi}$  are the generalized displacement, generalized velocity and generalized accelerated velocity of the carrier, respectively.

For the left side of Equation (7), the influence factors of the model are complex and coupled with each other. It is difficult to build an aerodynamic model that containing so many input parameters. For the right side, after decoupling, the physical significances of the models are clear and the modeling difficulty are reduced. Besides, the nonlinear relationships of the strong coupling parameters are considered as well. In this study, the fuzzy logic modeling method is employed to build the aerodynamic models such as  $F_1$  and  $F_2$ , and the linearized method is used to build the aerodynamic models  $F_3$ .

### (1) Models of $F_1$

The fuzzy logic modeling method is employed to build the models of  $F_1$ . The output of fuzzy logic model is expressed as [27]:

$$\hat{y}_j = \frac{\sum_{i=1}^n OP[A_1^i(x_{1j}), \dots, A_r^i(x_{rj}), \dots, A_k^i(x_{kj})] f_1^i(x_{1j}, x_{2j}, \dots, x_{kj})}{\sum_{i=1}^n OP[A_1^i(x_{1j}), \dots, A_r^i(x_{rj}), \dots, A_k^i(x_{kj})]} \quad (8)$$

where,  $\mathbf{x}_j = [x_{1j}, x_{2j}, \dots, x_{kj}]^T$  is the input of the model;  $k$  is the number of input parameters;  $n$  is the number of inner function;  $f_1^i(x_{1j}, x_{2j}, \dots, x_{kj})$  is the  $i$ th inner function;  $A_r^i(x_{rj})$  is the  $i$ th subordinate function of  $x_{rj}$ ;  $OP$  is the subordinate functions weighted operation. The models of  $F_1$  can be expressed as:

$$\begin{aligned} F_{z1}(\alpha, \theta, \dot{\theta}) &= \frac{\sum_{i=1}^n OP_1[A_1^i(\alpha), A_2^i(\theta), A_3^i(\dot{\theta})] f_1^i(\alpha, \theta, \dot{\theta})}{\sum_{i=1}^n OP_1[A_1^i(\alpha), A_2^i(\theta), A_3^i(\dot{\theta})]} \cdot qS \\ M_{y1}(\alpha, \theta, \dot{\theta}) &= \frac{\sum_{i=1}^n OP_2[A_1^i(\alpha), A_2^i(\theta), A_3^i(\dot{\theta})] f_2^i(\alpha, \theta, \dot{\theta})}{\sum_{i=1}^n OP_2[A_1^i(\alpha), A_2^i(\theta), A_3^i(\dot{\theta})]} \cdot qIS \end{aligned} \quad (9)$$

where,  $q$  denotes dynamic pressure of the free stream;  $l$  and  $S$  are the reference length and area of the aircraft, respectively.

(2) Models of  $F_2$ 

For the given carrier and spacecraft, the static deformation of the carrier  $\xi$  is a monotonic function of the relative distance between carrier and spacecraft  $c$ . That is:

$$\xi = f(c) \quad (10)$$

And then:

$$F_2(\xi, c) = F_2(f(c), c) = F_2(c) \quad (11)$$

With fuzzy logic modeling method, the models of  $F_2$  can be expressed as:

$$\begin{aligned} F_{z2}(c) &= \frac{\sum_{i=1}^n A^i(c) f_1^i(c)}{\sum_{i=1}^n A^i(c)} \cdot qS \\ M_{y2}(c) &= \frac{\sum_{i=1}^n A^i(c) f_2^i(c)}{\sum_{i=1}^n A^i(c)} \cdot qIS \end{aligned} \quad (12)$$

(3) Models of  $F_3(\xi, \dot{\xi}, \ddot{\xi}, c, t)$ 

$F_3(\xi, \dot{\xi}, \ddot{\xi}, c, t)$  is the interaction aerodynamics caused by the dynamic elastic deformation of the carrier, and can be considered as zero-mean-value of interference aerodynamic force. The model is expressed as Equation (13). There is a ratio relationship  $K$  between the zero-mean-value of aerodynamic coefficients responses of carrier and spacecraft,  $K$  is a function of relative distance  $c$  and is unrelated to physical time. Therefore, the input parameter  $c$  can be decoupled from the function  $F_{z,3}(\xi, \dot{\xi}, \ddot{\xi}, c, t)$ .

$$F_{z,3}(k) = K_{fz}(c) \cdot \left[ \sum_{i=1}^{na} \mathbf{A}'_i F_{z,3}(k-i) + \sum_{i=0}^{nb-1} \mathbf{B}'_i \xi(k-i) \right] \cdot qS \quad (13)$$

ARX model can be employed to construct the mappings of  $F_{z,3}(\xi, \dot{\xi}, \ddot{\xi}, t)$ . As the second derivative of generalized displacement is considered, the delay order of input is  $nb = 3$ . The feedback of the model is ignored and  $na = 0$ . Equation (13) is simplified as:

$$F_{z,3}(k) = K_{fz}(c) \cdot [\mathbf{B}'_0 \xi(k) + \mathbf{B}'_1 \xi(k-1) + \mathbf{B}'_2 \xi(k-2)] \cdot qS \quad (14)$$

The continuous form of Equation (14) is:

$$F_{z,3}(\xi, \dot{\xi}, \ddot{\xi}, c, t) = K_{fz}(c) \cdot [\mathbf{B}_{10} \xi(t) + \mathbf{B}_{11} \dot{\xi}(t) + \mathbf{B}_{12} \ddot{\xi}(t)] \cdot qS \quad (15)$$

The interference aerodynamic pitching moment model of the spacecraft caused by the dynamic elastic deformation of the carrier is expressed as:

$$M_{y,3}(\xi, \dot{\xi}, \ddot{\xi}, c, t) = K_{my}(c) \cdot (\mathbf{B}_{20} \xi(t) + \mathbf{B}_{21} \dot{\xi}(t) + \mathbf{B}_{22} \ddot{\xi}(t)) \cdot qIS \quad (16)$$

## (4) Models of spacecraft

Bring Equation (9), (12), (15), (16) into Equation (7), the aerodynamic models of spacecraft can be expressed as:

$$\begin{aligned} F_z(\alpha, \theta, q, \xi, \dot{\xi}, \ddot{\xi}, c, t) &= \frac{\sum_{i=1}^n OP_1[A_1^i(\alpha), A_2^i(\theta), A_3^i(\dot{\theta})] f_1^i(\alpha, \theta, \dot{\theta})}{\sum_{i=1}^n OP_1[A_1^i(\alpha), A_2^i(\theta), A_3^i(\dot{\theta})]} \cdot qS + K_{fz}(c) \cdot [\mathbf{B}_{10} \quad \mathbf{B}_{11} \quad \mathbf{B}_{12}] [\xi \quad \dot{\xi} \quad \ddot{\xi}]^T \cdot qS \\ &\quad + \frac{\sum_{i=1}^n A^i(c) f_1^i(c)}{\sum_{i=1}^n A^i(c)} \cdot qS \\ M_y(\alpha, \theta, q, \xi, \dot{\xi}, \ddot{\xi}, c, t) &= \frac{\sum_{i=1}^n OP_2[A_1^i(\alpha), A_2^i(\theta), A_3^i(\dot{\theta})] f_2^i(\alpha, \theta, \dot{\theta})}{\sum_{i=1}^n OP_2[A_1^i(\alpha), A_2^i(\theta), A_3^i(\dot{\theta})]} \cdot qIS + K_{my}(c) \cdot [\mathbf{B}_{20} \quad \mathbf{B}_{21} \quad \mathbf{B}_{22}] [\xi \quad \dot{\xi} \quad \ddot{\xi}]^T \cdot qIS \\ &\quad + \frac{\sum_{i=1}^n A^i(c) f_2^i(c)}{\sum_{i=1}^n A^i(c)} \cdot qIS \end{aligned} \quad (17)$$

## 2.4. The kinetic equation group

In Equation (4), the structure dynamic equation of carrier is [26]:

$$\mathbf{M} \ddot{\xi} + \mathbf{G} \dot{\xi} + \mathbf{K} \xi = \mathbf{F}_a(\xi, \dot{\xi}, t) = q \cdot \mathbf{f}_a(\xi, \dot{\xi}, t) \quad (18)$$

where,  $q$  is dynamic pressure of the free stream. The state-space form of the equation (18) is expressed as:

$$\begin{bmatrix} \dot{\xi} \\ \xi \end{bmatrix} = \begin{bmatrix} 0 & I \\ -\mathbf{M}^{-1} \mathbf{K} & -\mathbf{M}^{-1} \mathbf{G} \end{bmatrix} \begin{bmatrix} \xi \\ \dot{\xi} \end{bmatrix} + q \begin{bmatrix} 0 \\ \mathbf{M}^{-1} \end{bmatrix} \mathbf{f}_a(\xi, \dot{\xi}, t) \quad (19)$$

Let's:

$$\mathbf{x}_s = \begin{bmatrix} \xi \\ \dot{\xi} \end{bmatrix}, \quad \mathbf{A}_s = \begin{bmatrix} 0 & I \\ -\mathbf{M}^{-1}\mathbf{K} & -\mathbf{M}^{-1}\mathbf{G} \end{bmatrix}, \quad \mathbf{B}_s = \begin{bmatrix} 0 \\ \mathbf{M}^{-1} \end{bmatrix}$$

The structure dynamic equation of the carrier in continuous form is:

$$\dot{\mathbf{x}}_s(t) = \mathbf{A}_s \mathbf{x}_s(t) + q \mathbf{B}_s \mathbf{f}_q(t) \quad (20)$$

Due to the equation:

$$\mathbf{x}_b(t) = \begin{bmatrix} 1 & 0 \end{bmatrix} \mathbf{x}_s(t) = \mathbf{C}_s \mathbf{x}_s(t) \quad (21)$$

By considering the equations (6), (20) and (21), we get Equations (22):

$$\begin{cases} \dot{\mathbf{x}}_s(t) = (\mathbf{A}_s + q\mathbf{B}_s\mathbf{D}_a\mathbf{C}_s)\mathbf{x}_s(t) + q\mathbf{B}_s\mathbf{C}_a\mathbf{x}_a(t) + q\mathbf{B}_s\mathbf{f}_{a0} \\ \dot{\mathbf{x}}_a(t) = \mathbf{A}_a\mathbf{x}_a(t) + \mathbf{B}_a\mathbf{C}_s\mathbf{x}_s(t) \end{cases} \quad (22)$$

By considering the equations (3) and (17), the rigid body dynamic equation of spacecraft is:

$$\left\{ \begin{aligned} m\ddot{\mathbf{z}} &= \frac{\sum_{i=1}^n OP_1[A_1^i(\alpha), A_2^i(\theta), A_3^i(\dot{\theta})]f_1^i(\alpha, \theta, \dot{\theta})}{\sum_{i=1}^n OP_1[A_1^i(\alpha), A_2^i(\theta), A_3^i(\dot{\theta})]} \cdot qS + K_{fz}(c) \cdot [\mathbf{B}_{10} \quad \mathbf{B}_{11} \quad \mathbf{B}_{12}] [\xi \quad \dot{\xi} \quad \ddot{\xi}]^T \cdot qS \\ &\quad + \frac{\sum_{i=1}^n A^i(c)f_1^i(c)}{\sum_{i=1}^n A^i(c)} \cdot qS - mg \cos \theta \\ I_y \ddot{\theta} &= \frac{\sum_{i=1}^n OP_2[A_1^i(\alpha), A_2^i(\theta), A_3^i(\dot{\theta})]f_2^i(\alpha, \theta, \dot{\theta})}{\sum_{i=1}^n OP_2[A_1^i(\alpha), A_2^i(\theta), A_3^i(\dot{\theta})]} \cdot qLS + K_{my}(c) \cdot [\mathbf{B}_{20} \quad \mathbf{B}_{21} \quad \mathbf{B}_{22}] [\xi \quad \dot{\xi} \quad \ddot{\xi}]^T \cdot qLS + \frac{\sum_{i=1}^n A^i(c)f_2^i(c)}{\sum_{i=1}^n A^i(c)} \cdot qLS \end{aligned} \right. \quad (23)$$

Let's:

$$\mathbf{P}_1 = \mathbf{A}_s + q\mathbf{B}_s\mathbf{D}_a\mathbf{C}_s, \quad \mathbf{P}_2 = q\mathbf{B}_s\mathbf{C}_a, \quad \mathbf{P}_3 = q\mathbf{B}_s$$

The first equation in simultaneous equations (22) is expressed as:

$$\begin{bmatrix} \dot{\xi} \\ \ddot{\xi} \end{bmatrix} = \mathbf{P}_1 \begin{bmatrix} \xi \\ \dot{\xi} \end{bmatrix} + \mathbf{P}_2 \mathbf{x}_a(t) + \mathbf{P}_3 \mathbf{f}_{a0} = \begin{bmatrix} \mathbf{P}_{11} & \mathbf{P}_{12} \\ \mathbf{P}_{13} & \mathbf{P}_{14} \end{bmatrix} \begin{bmatrix} \xi \\ \dot{\xi} \end{bmatrix} + \begin{bmatrix} \mathbf{P}_{21} \\ \mathbf{P}_{22} \end{bmatrix} \mathbf{x}_a(t) + \begin{bmatrix} \mathbf{P}_{31} \\ \mathbf{P}_{32} \end{bmatrix} \mathbf{f}_{a0} \quad (24)$$

And then:

$$\ddot{\xi} = \mathbf{P}_{13}\xi + \mathbf{P}_{14}\dot{\xi} + \mathbf{P}_{22}\mathbf{x}_a(t) + \mathbf{P}_{32}\mathbf{f}_{a0} \quad (25)$$

By considering the equations (22), (23) and (25), we get simultaneous equations (26), which are the governing equation of the store separation problem considering the elastic deformation of the carrier.

$$\begin{cases} \dot{\mathbf{x}}_s(t) = (\mathbf{A}_s + q\mathbf{B}_s\mathbf{D}_a\mathbf{C}_s)\mathbf{x}_s(t) + q\mathbf{B}_s\mathbf{C}_a\mathbf{x}_a(t) + q\mathbf{B}_s\mathbf{f}_{a0} \\ \dot{\mathbf{x}}_a(t) = \mathbf{A}_a\mathbf{x}_a(t) + \mathbf{B}_a\mathbf{C}_s\mathbf{x}_s(t) \\ m\ddot{z} = F_{z1}(\alpha, \theta, \dot{\theta}) + K_{fz}(c) \cdot [(\mathbf{B}_{10} + \mathbf{B}_{12}\mathbf{P}_{13})\dot{\xi} + (\mathbf{B}_{11} + \mathbf{B}_{12}\mathbf{P}_{14})\dot{\xi} + \mathbf{B}_{12}\mathbf{P}_{22}\mathbf{x}_a(t) + \mathbf{B}_{12}\mathbf{P}_{32}\mathbf{f}_{a0}] + F_{z0}(c) - mg \cos \theta \\ I_y\ddot{\theta} = M_{y1}(\alpha, \theta, \dot{\theta}) + K_{my}(c) \cdot [(\mathbf{B}_{20} + \mathbf{B}_{22}\mathbf{P}_{13})\dot{\xi} + (\mathbf{B}_{21} + \mathbf{B}_{22}\mathbf{P}_{14})\dot{\xi} + \mathbf{B}_{22}\mathbf{P}_{22}\mathbf{x}_a(t) + \mathbf{B}_{22}\mathbf{P}_{32}\mathbf{f}_{a0}] + M_{y0}(c) \end{cases} \quad (26)$$

where:

$$F_{z1}(\alpha, \theta, \dot{\theta}) = \frac{\sum_{i=1}^n OP_1[A_1^i(\alpha), A_2^i(\theta), A_3^i(\dot{\theta})]f_1^i(\alpha, \theta, \dot{\theta})}{\sum_{i=1}^n OP_1[A_1^i(\alpha), A_2^i(\theta), A_3^i(\dot{\theta})]} \cdot qS, F_{z2}(c) = \frac{\sum_{i=1}^n A^i(c)f_1^i(c)}{\sum_{i=1}^n A^i(c)} \cdot qS$$

$$M_{y1}(\alpha, \theta, \dot{\theta}) = \frac{\sum_{i=1}^n OP_2[A_1^i(\alpha), A_2^i(\theta), A_3^i(\dot{\theta})]f_2^i(\alpha, \theta, \dot{\theta})}{\sum_{i=1}^n OP_2[A_1^i(\alpha), A_2^i(\theta), A_3^i(\dot{\theta})]} \cdot qIS, M_{y2}(c) = \frac{\sum_{i=1}^n A^i(c)f_2^i(c)}{\sum_{i=1}^n A^i(c)} \cdot qIS$$

### 3. Aircraft model and calculation status

In this study, the carrier aircraft is simplified to an elastic wing (AGARD445.6) [28]. The modal method is employed to build the structural model. As the vibration characteristics of the AGARD445.6 wing mainly depend on the first four modes of vibration, the first four order modes are considered. The hybrid unstructured grid is used for spatial discretization. The grids near the wall are prism cells and the others are tetrahedral cells. The surface cell number is 35 thousands and the volume cell number is 1.1 millions. Fig. 1 shows the surface grids of initial state.

The spacecraft is simplified to a rigid delta wing aircraft with a vertical tail. As shown in Fig. 2, the fuselage of spacecraft is revolution body with a length of 800 mm and a diameter of 60 mm. The wingspan is 364 mm and the sweep angle is  $70^\circ$ . The distance between

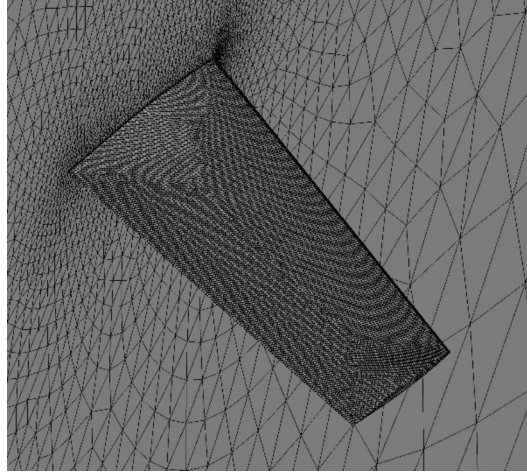


Fig. 1. Surface grid of AGARD445.6 wing.

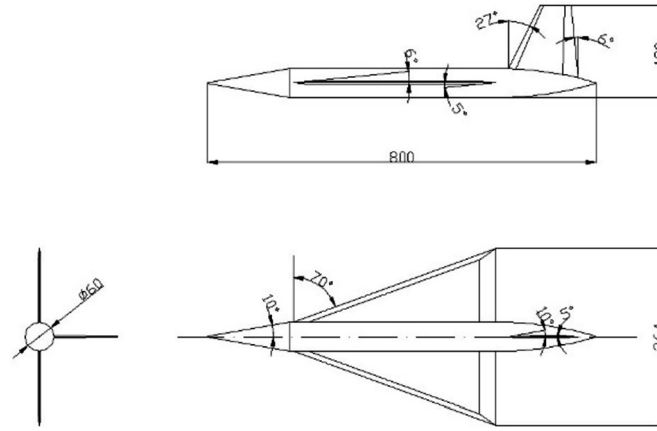


Fig. 2. The three view drawing of the spacecraft.

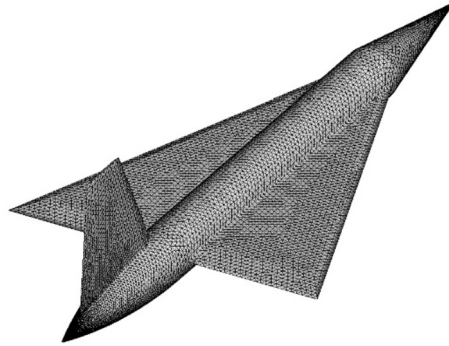


Fig. 3. Surface grid of the spacecraft.

the mass center and nose is 300 mm. The mass of the spacecraft is 4.124 kg, the principal moments of inertia along the x, y and z axis are  $0.009 \text{ kg/m}^2$ ,  $0.122 \text{ kg/m}^2$  and  $0.126 \text{ kg/m}^2$  respectively. The products of inertia  $I_{xz}$  is  $-0.002 \text{ kg/m}^2$ . Fig. 3 shows the surface grids of spacecraft. The surface cell number is 30 thousands and the volume cell number is 0.61 millions.

The simulation settings are as follows: the separation altitude is 15 km, the incoming flow Mach number is 0.7 and the attack angle is 2 deg. The Reynolds number based on the mean aerodynamic chord of the carrier is  $1.58\text{e}6$ .

The GFSI (generalized fluid-structure interaction) solver developed by our research group is used in this study, which is a multidisciplinary coupled solver containing CFD (computational fluid dynamics), CSD (computational structure dynamics) and RBD (rigid body dynamics) modules [29–31]. On the one hand, the input-output data of training and verifying samples for ROM are calculated with GFSI. On the other hand, with GFSI solver, the CFD/CSD/RBD coupling simulations are carried out, and the results are used to verify the predictions of ROM/CSD/RBD coupling simulation method. The GFSI solver has been got sufficient verification, and with higher calculation accuracy [29–36].



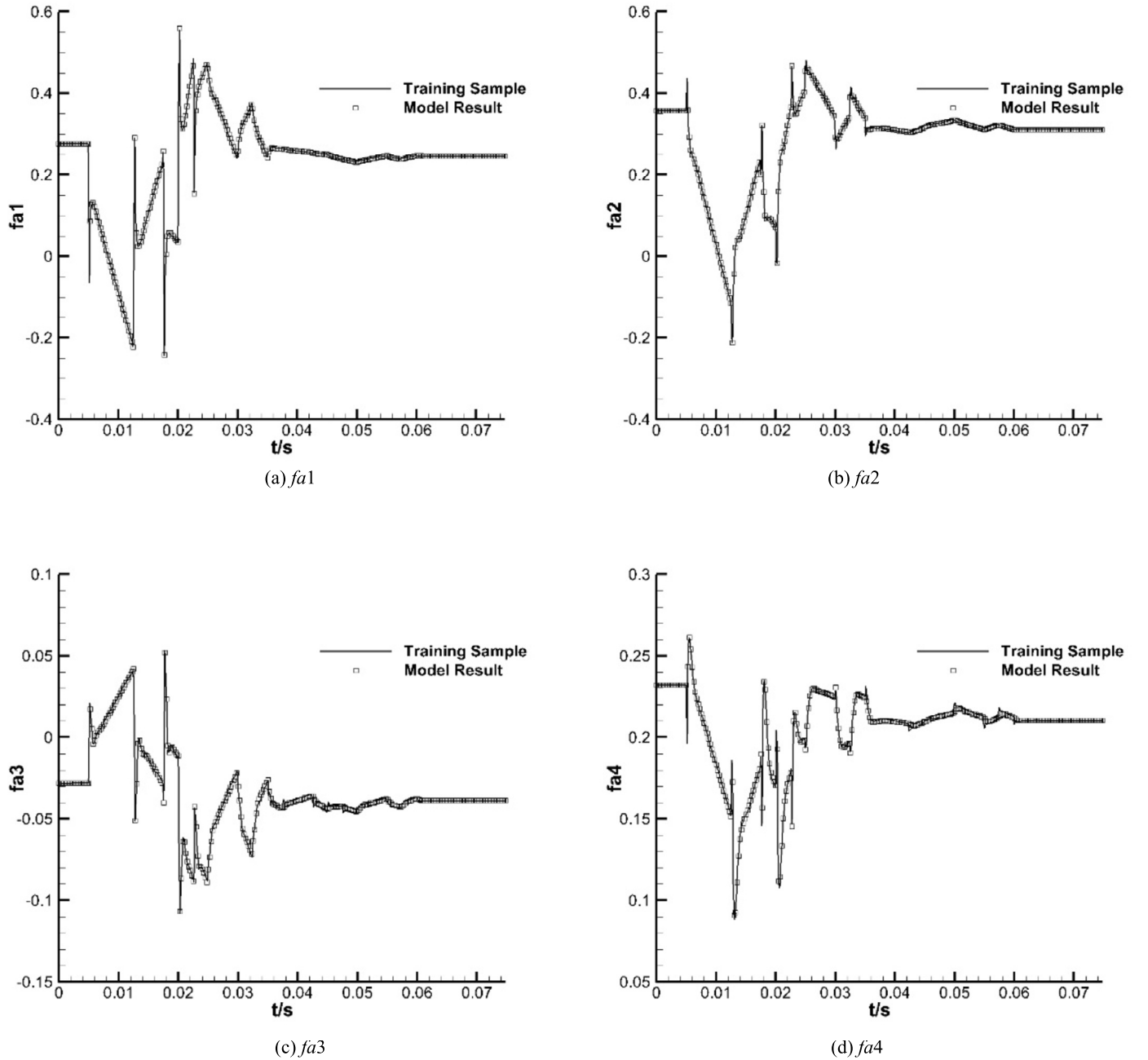


Fig. 4. Generalized aerodynamic forces of the carrier (Comparison between model results and the training samples).

For the CFD setting, the S-A turbulence model is employed to enclose the N-S equations, and the dual-time stepping method is used. The Gauss-Seidel method is utilized for pseudo time marching and AUSM+ scheme is used for spatial discretization. Besides, the nested grid and grid deformation methods are employed during the unsteady multidisciplinary coupled simulation.

#### 4. Identification and verification of aerodynamic model

##### 4.1. Generalized aerodynamic model of carrier

For the elastic carrier, the generalized displacements and generalized aerodynamic forces responses are the inputs and outputs of the aerodynamic models. During the modeling, the inputs of the training samples are designed with the “3211” signal. By solving the unsteady Navier-Stokes equation with the GFSI code, the outputs of the training samples are calculated. The delay order of the input and feedback of the model are all four, and the least square method is employed to identify model parameters. As a consequence, the model results and the training samples are compared in Fig. 4. As we can see, the model results are in good agreement with the training samples.

The free vibration responses of the carrier are calculated by CFD/CSD method. The dynamic responses are taken as the verifying samples to test the generalized aerodynamic model. As shown in Fig. 5, the model results agree fairly well with the verifying samples. The generalized aerodynamic model of the carrier has high precision.

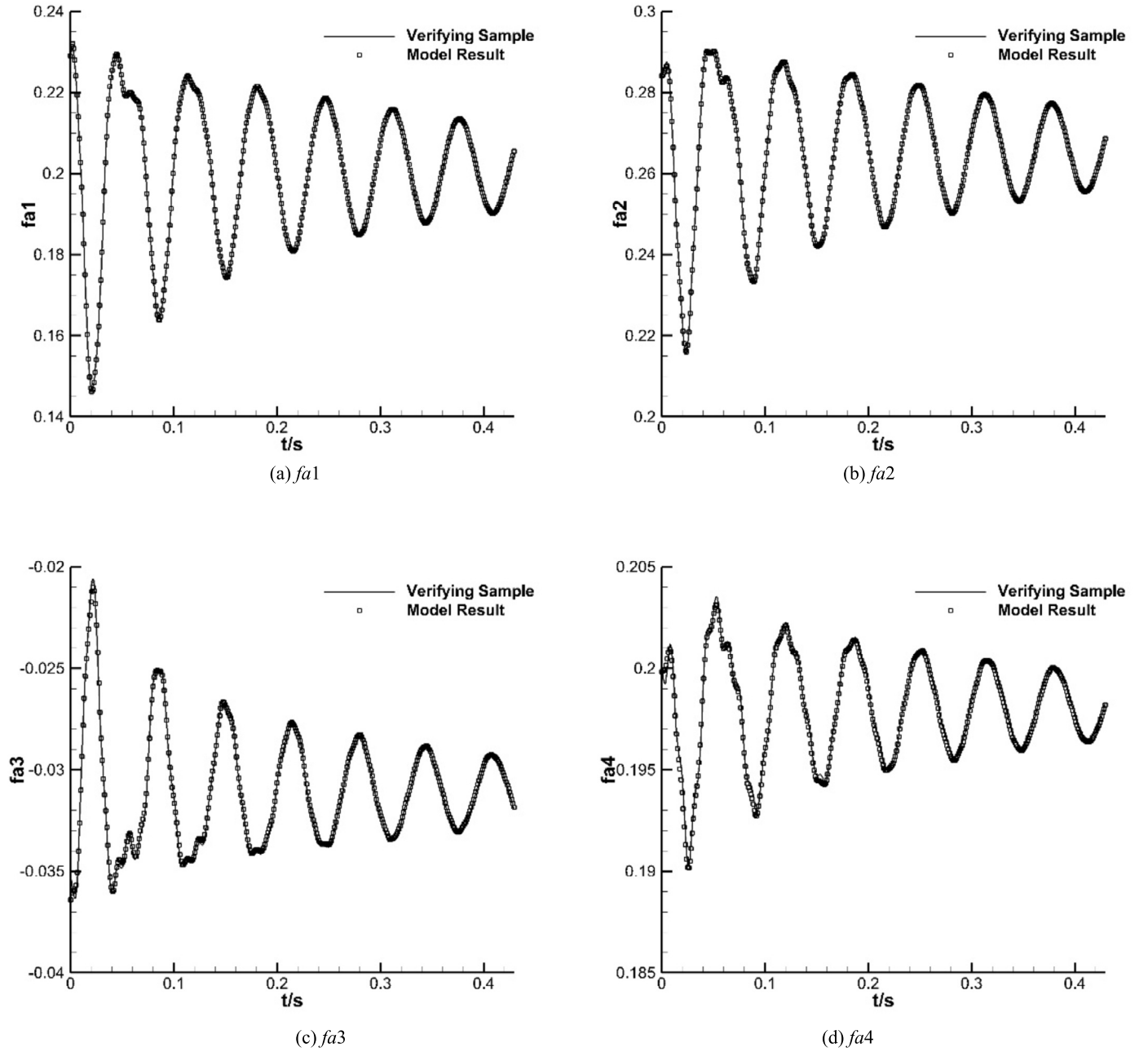


Fig. 5. Generalized aerodynamic forces of the carrier (Comparison between model results and the verifying samples).

**Table 1**  
Aerodynamic coefficient models.

Model	$\alpha$	$\theta$	$\dot{\theta}$	Fuzzy unit number	Correlation coefficient
Normal force	1	2	1	3	0.9994496
Pitching moment	1	2	1	3	0.9991180

#### 4.2. Aerodynamic model $F_1$ of spacecraft

During separation, the Mach number and flight altitude are nearly invariable. The inputs parameters of the model include angle of attack  $\alpha$ , pitching angle  $\theta$  and pitching rate  $\dot{\theta}$ . The inputs of the training samples are designed with sweep signal as shown in Fig. 6. It is important to note that the frequency range of the training signals should include the short period mode frequency of spacecraft. The outputs of training samples are calculated by unsteady CFD method.

The aerodynamic models of the spacecraft are built with fuzzy logic method. By identification, the model structure and correlation coefficients are shown in Table 1. The correlation coefficients of the models are all above 0.999. The comparisons between aerodynamic models and the training samples are shown in Fig. 7. As we can see, the aerodynamic models results agree well with the training samples.



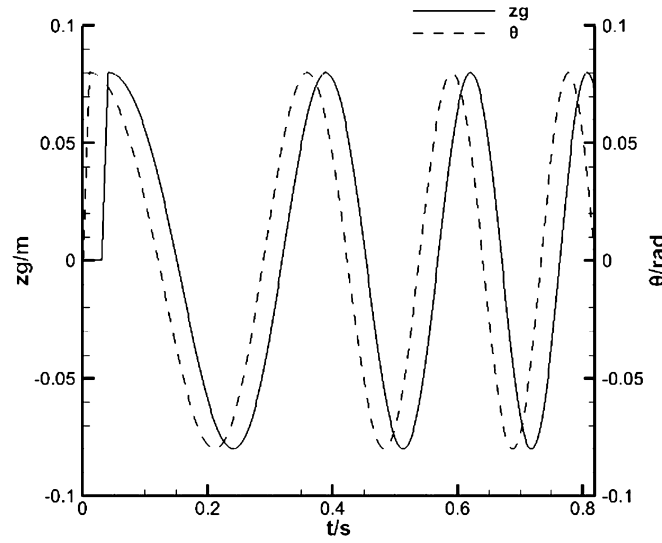


Fig. 6. Training sample of the aerodynamic model of spacecraft.

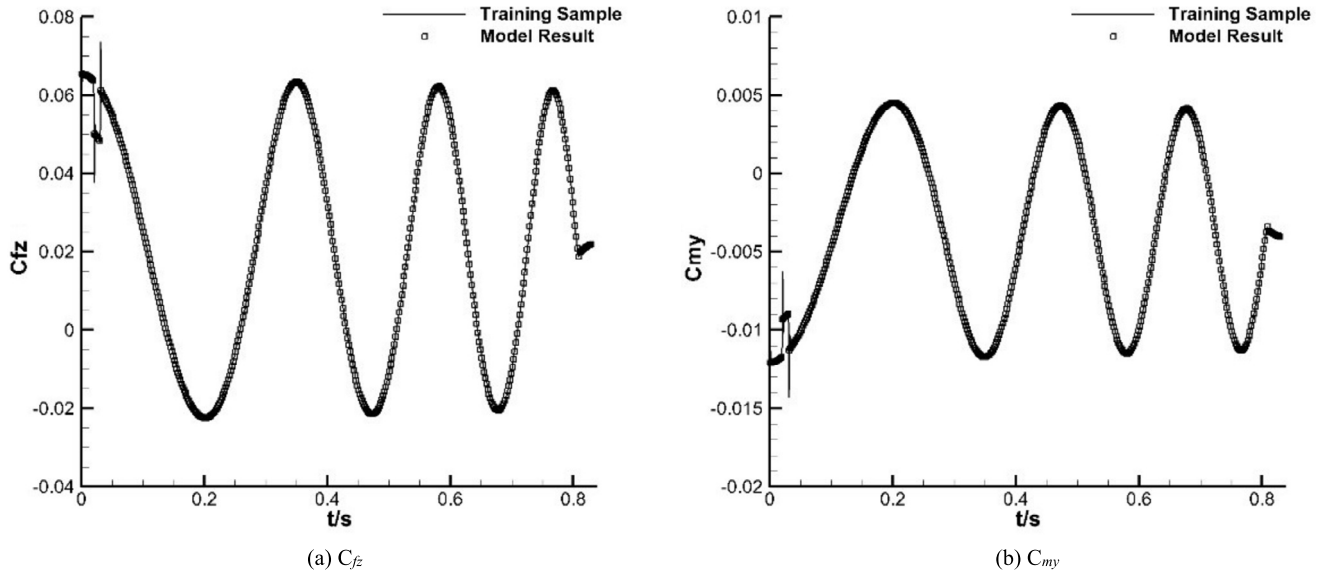


Fig. 7. Comparison between aerodynamic model based on sweep signal and the training samples.

The verifying samples are dynamic responses of pitching/plunging two degrees of freedom free flight of spacecraft, which are simulated by CFD/RBD coupling method. The comparisons between the aerodynamic model results and verifying samples are shown in Fig. 8. As we can see, the model output has high precision.

In order to verify the accuracies of the aerodynamic models further, the ROM based pitching/plunging two degrees of freedom simulation is performed. The Runge-Kutta method is employed in the simulations. Primarily, the time step convergence of the ROM/RBD system is studied, and the time steps of 0.01 s, 0.001 s and 0.0001 s are considered. The simulation results are shown in Fig. 9, the time step has little influence on the normal displacement and pitching angle responses of spacecraft. And when the time steps are 0.001 s and 0.0001 s, the simulation results are almost the same. Therefore, the time step of 0.001 s is employed.

The ROM/RBD simulation results are shown in Fig. 10, which basically agree well with that of the CFD/RBD results. The pitch angle response has a slight error after 0.6 s. The accuracy of aerodynamic models satisfies the simulation requirements.

#### 4.3. Interference aerodynamic model $F_3$ of spacecraft

For model  $F_3$ , the variable  $c$  can be decoupled with generalized displacement of carrier [7]. When the real distance between the carrier aircraft and the central axis of the spacecraft is 0.25 m, defined the relative distance  $c$  is 0, and the scale factor is 1. Thus:

$$K(0) = 1 \quad (27)$$

Then the aerodynamic models  $F_3$  can be expressed as:

$$\begin{aligned} F_{z3}(\xi, \dot{\xi}, \ddot{\xi}, c, t) &= K_{fz}(c) \cdot F_{z3}(\xi, \dot{\xi}, \ddot{\xi}, t) = K_{fz}(c) \cdot F_{z3}(\xi, \dot{\xi}, \ddot{\xi}, 0, t) \\ M_{y3}(\xi, \dot{\xi}, \ddot{\xi}, c, t) &= K_{my}(c) \cdot M_{y3}(\xi, \dot{\xi}, \ddot{\xi}, t) = K_{my}(c) \cdot M_{y3}(\xi, \dot{\xi}, \ddot{\xi}, 0, t) \end{aligned} \quad (28)$$

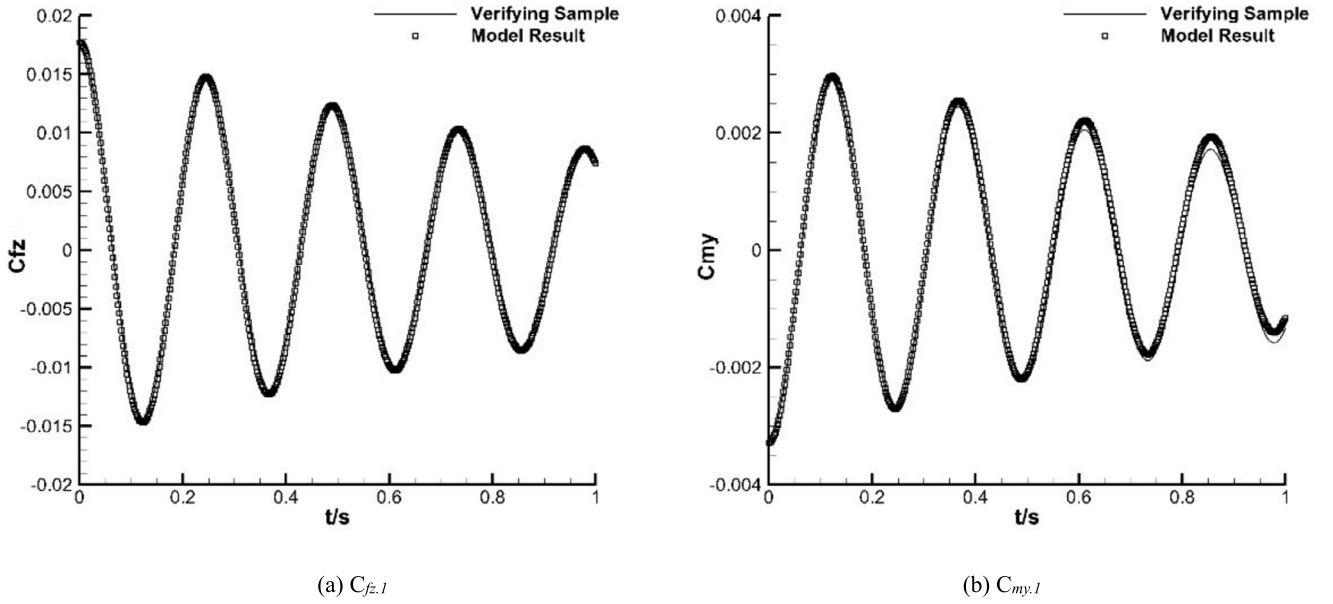


Fig. 8. Comparison between aerodynamic model based on sweep signal and the verifying samples.

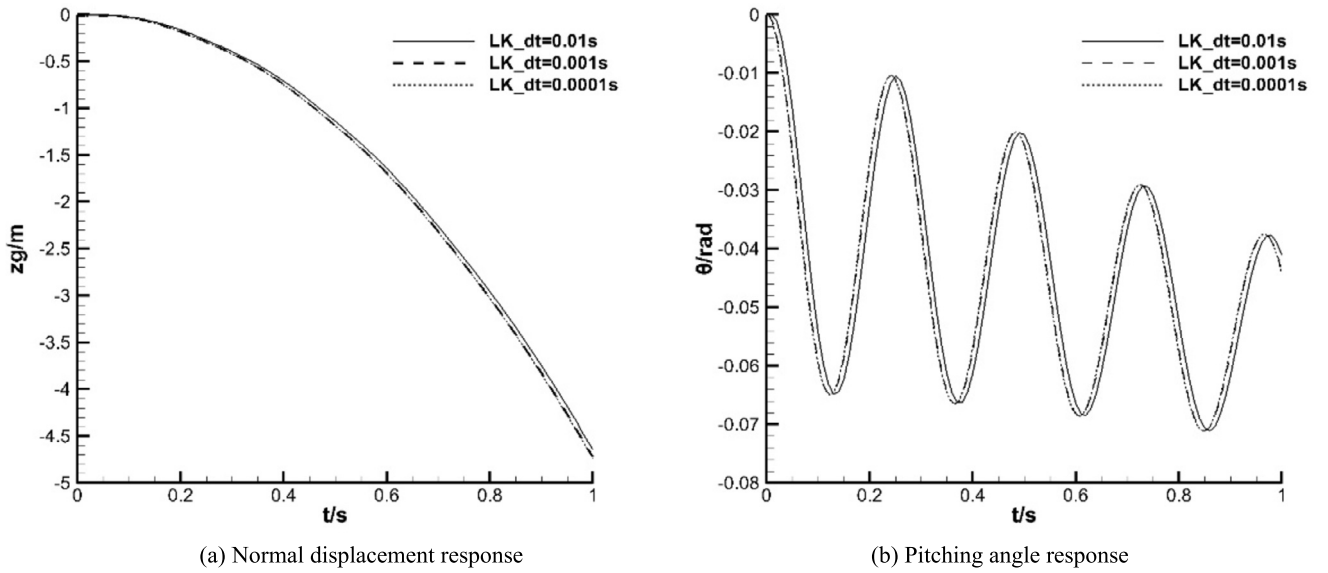


Fig. 9. Time step convergence study.

It is observed that the aerodynamic model can be divided into two parts. One part is the aerodynamic models when the relative distance is 0. The other is the scale factor model.

The training samples are solved by CFD/CSD simulation method. The calculation steps are as follows. Firstly, fixing spacecraft at a relative distance  $c = 0$  under the carrier wing. Secondly, a concentrated load is applied on the elastic carrier. The magnitude of the load equals to the gravity of spacecraft. Thirdly, calculating the static deformation of carrier under the aerodynamic load and concentrated load. Fourthly, the concentrated load disappears instantaneously, which simulates the uploading of spacecraft during separates. Finally, calculating the dynamic responses of carrier and the unsteady aerodynamic forces of spacecraft.

Through calculation, the generalized displacement responses of carrier are shown in Fig. 11, the aerodynamic force coefficient responses of spacecraft are shown in Fig. 12. It is obvious that the static deformation of the carrier has been converged at about 0.016 s, and spacecraft separate from carrier at about 0.0175 s. As shown in Fig. 12, under the interference of the elastic wing, the normal force and pitching moment coefficient responses of spacecraft change periodically, and convergence trend and frequency are same with the generalized displacement responses of the carrier.

In Fig. 12(b), under the influence of the static deformation of carrier, the pitching moment coefficient of spacecraft is  $C_{my,1} + C_{my,2}(0) = -0.00168722$ , which is the mean value of the pitching moment coefficient. Consider  $C_{my,1} = -0.00320463$ , the mean value of the interference pitching moment coefficient  $C_{my,2}(0) = 0.00151741$ . The generalized displacement responses of carrier at the first 0.1 s are used as the inputs of training sample, and the corresponding zero-averaged pitching moment coefficient responses of spacecraft are outputs. The aerodynamic model  $C_{my,3}$  are identified by least squares method. The normal force coefficient model  $C_{fz,3}$  is established in the same way. The comparisons between CFD and model results are shown in Fig. 13. As we can see, the model results agree well with CFD.

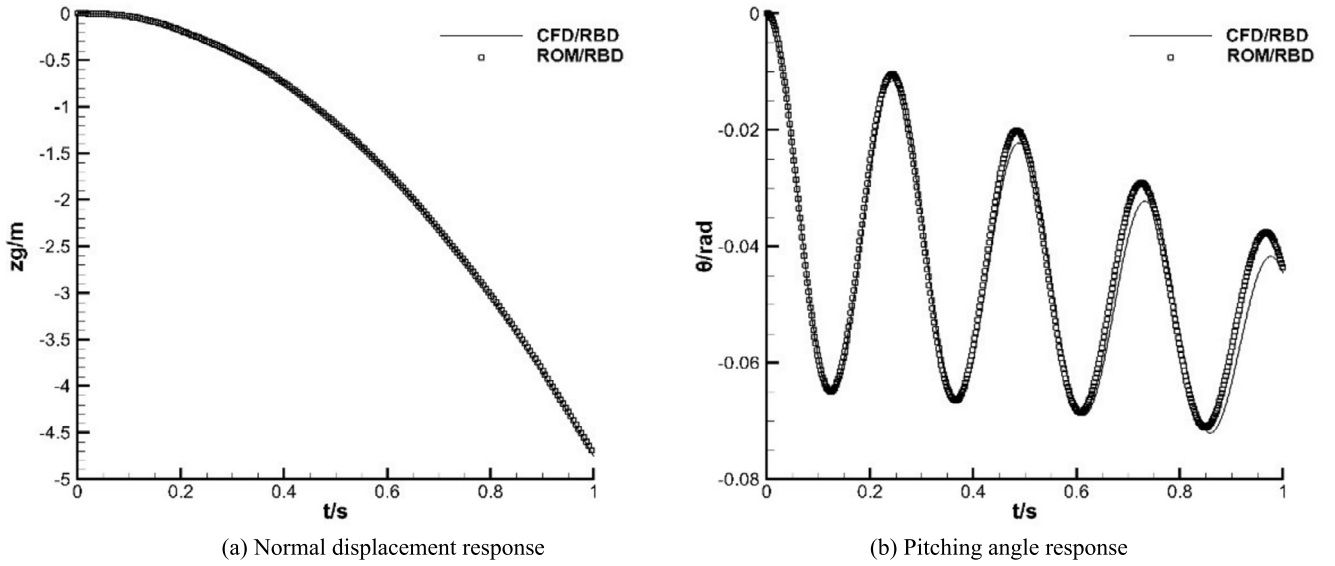


Fig. 10. The ROM/RBD simulation results based on sweep signal.

Table 2

The scale factor K.

$c$	0C	0.3C	0.5C	1.0C	2.0C
$C_{fz,3}$ ( $t=0.016$ s)	-0.00257	-0.00147	-0.00112	-0.00066	-0.00033
$K_{fz}$	1	0.572363	0.434645	0.257598	0.129297
$C_{my,3}$ ( $t=0.016$ s)	0.000598	0.000302	0.000215	0.000114	5.23E-05
$K_{my}$	1	0.504534	0.359125	0.190031	0.087486

Table 3

Relative errors.

$t/s$	$0.3C_{fz}$	$0.3C_{my}$	$0.5C_{fz}$	$0.5C_{my}$
0.1	3.52%	1.50%	5.38%	1.54%
0.2	2.84%	0.99%	6.11%	0.63%
0.3	4.03%	0.44%	10.74%	4.74%
0.4	4.73%	1.62%	10.53%	2.60%

For the scale factor model, the training samples are solved through CFD/CSD method. The calculation steps are as follows. Firstly, fixing spacecraft at different positions from the carrier. The relative distances of  $c = 0, 0.3C, 0.5C, 1.0C$  and  $2.0C$  are considered. Secondly, calculating the aerodynamic responses of spacecraft during dynamic elastic deformation of carrier. Finally, calculating the zero-averaged aerodynamic responses. During the simulation, the physical time step is  $0.000546181$  s, which is the  $1/20$  of the highest-order modal frequency of carrier. The physical simulation time is  $0.02$  s.

The zero-mean values of the interference aerodynamic coefficients of spacecraft are shown in Fig. 14. And the scale factor  $K$  is calculated in Table 2. With the relative distances and scale factors as the input and output of training samples, the scale factor models are established by polynomial curve fitting. The models are expressed as Equation (29). The comparisons between the model results and training samples are shown in Fig. 15. It can be seen that the models have high precision.

$$\begin{aligned}
 K_{fz}(c) &= 1 / \left[ -0.0473 (c/C)^3 + 0.6275 (c/C)^2 + 2.3013 (c/C) + 1.0003 \right] \\
 K_{my}(c) &= 1 / \left[ -0.28 (c/C)^3 + 1.7941 (c/C)^2 + 2.7467 (c/C) + 1.0008 \right]
 \end{aligned} \quad (29)$$

The interference aerodynamic models  $F_3$  are all established above. In order to validate the models further, the research steps are as follows. Firstly, calculating the interference aerodynamics of spacecraft and dynamic responses of the carrier with different relative distances by CFD/CSD method. Secondly, employing the generalized displacement responses of the carrier and relative distance as input parameters, and calculating the interference aerodynamics of the spacecraft with aerodynamic models. The comparisons between model and CFD/CSD results with different relative distances are shown in Fig. 16 and Fig. 17. As we can see, when the relative distance is  $0.3C$  and  $0.5C$ , the output of the models agrees well with the CFD/CSD results. The relative errors are shown in Table 3. When the relative distance is  $0.3C$ , the maximum relative error of  $C_{fz}$  and  $C_{my}$  are less than 5% and 2% respectively. And when the relative distance is  $0.5C$ , the maximum relative error of  $C_{fz}$  and  $C_{my}$  are less than 11% and 5% respectively.

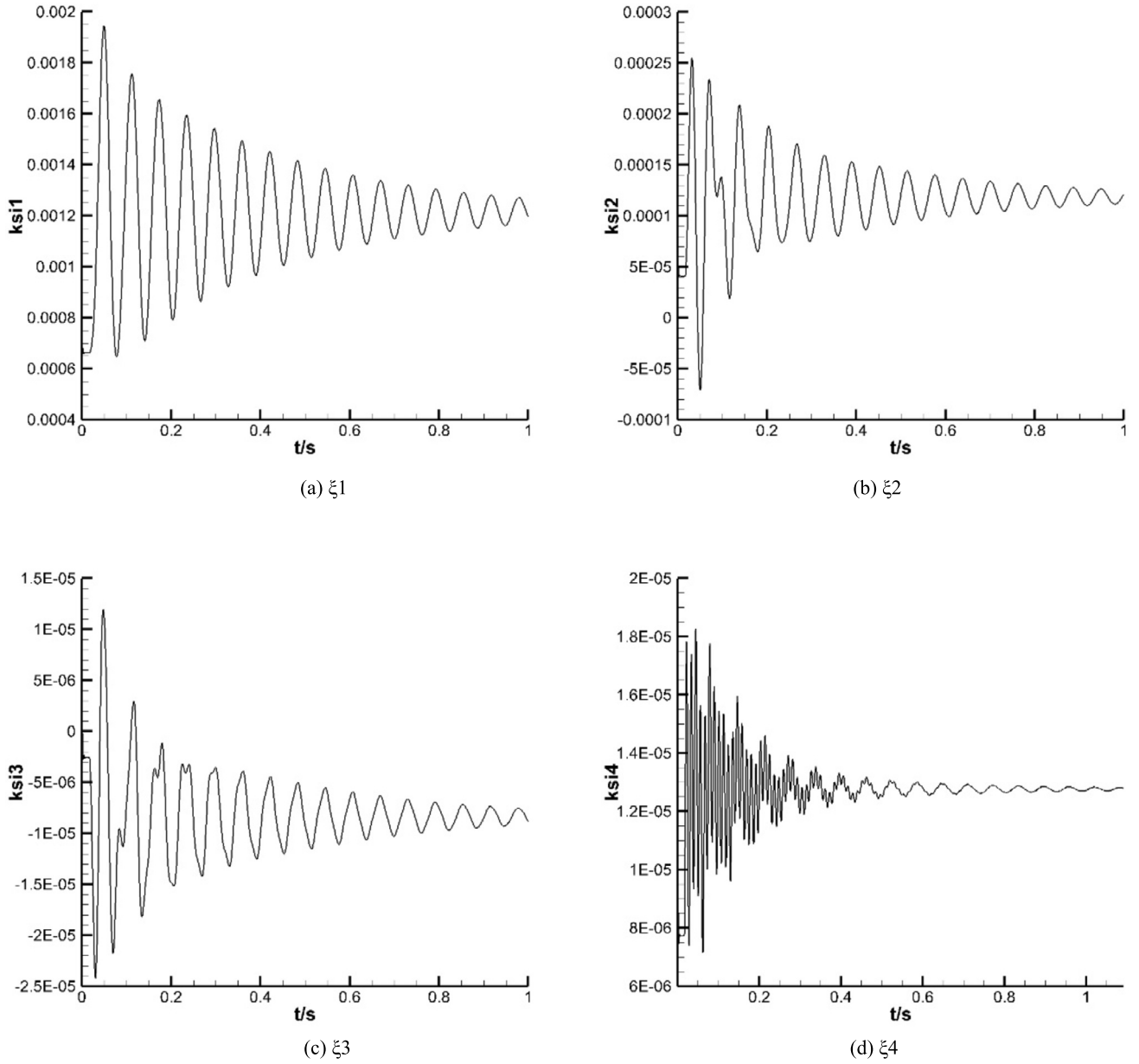


Fig. 11. The generalized displacement responses of the carrier.

Table 4

The mean values of the interference aerodynamics coefficients under different relative distances.

c	0C	0.3C	0.5C	1.0C	2.0C
$C_{fz,2}$	-0.002408	-0.001972	-0.001704	-0.001347	-0.000616
$C_{my,2}$	0.001517	0.001490	0.001426	0.001288	0.000916

#### 4.4. Interference aerodynamic model $F_2$ of spacecraft

Through the above simulation, the mean values of the interference aerodynamics coefficients of spacecraft under different relative distances are extracted and shown in Table 4, which are the training samples of model  $F_2$ . The fuzzy logic method is employed. Through identification, the model structure and correlation coefficients are shown in Table 5, and the correlation coefficients of the models are all above 0.99. The comparisons between aerodynamic models and CFD/CSD results are shown in Fig. 18. As we can see, the models outputs fit the CFD/CSD results well.

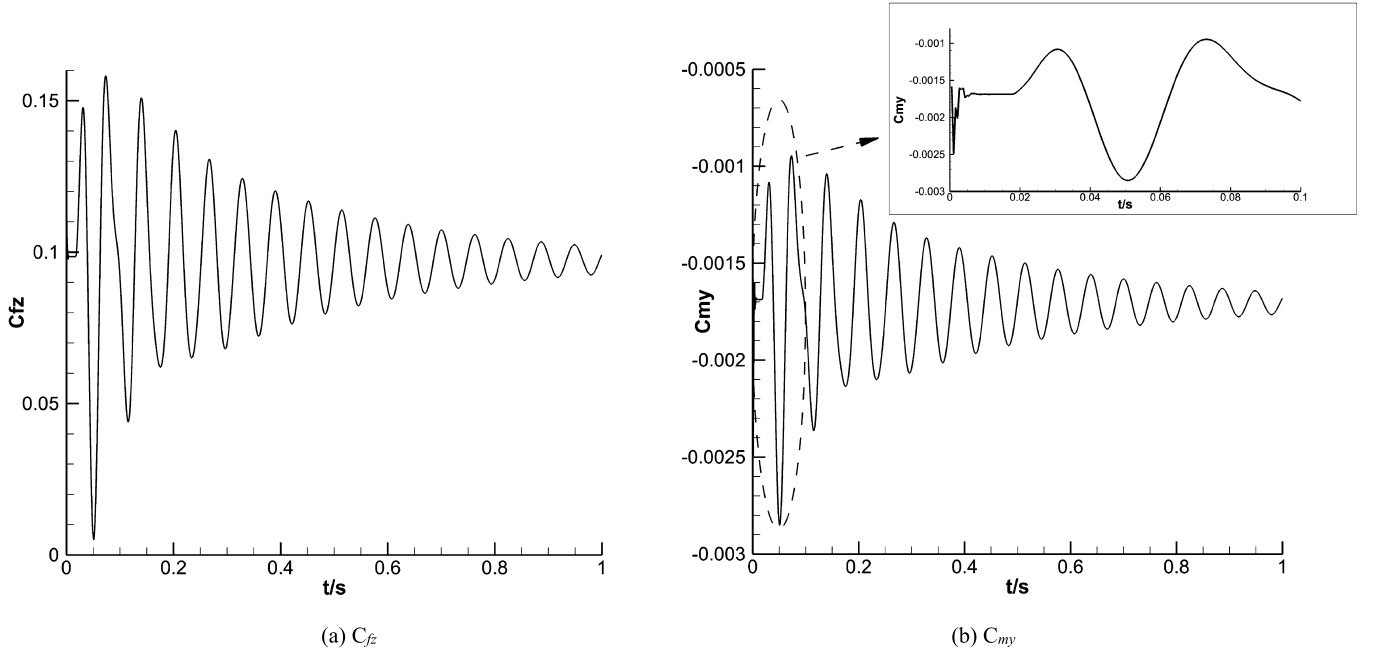


Fig. 12. The aerodynamic forces responses of the spacecraft.

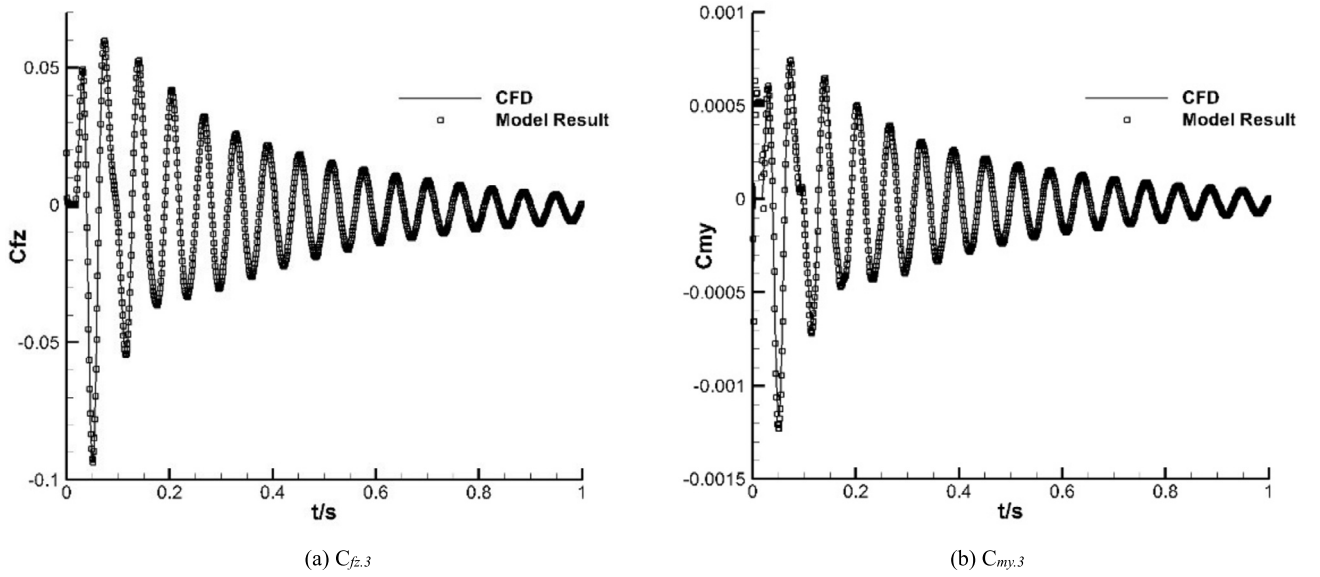


Fig. 13. Comparison between aerodynamic model results and CFD.

Table 5

The model structure of the  $C_{f,2}$ .

Model	$c/C$	Fuzzy unit number	Correlation coefficient
$C_{fz,2}$	2	2	0.9915309
$C_{my,2}$	2	2	0.9907893

## 5. Dynamics simulation and analysis

### 5.1. Baseline case

In order to verify the accuracy and applicability of the aerodynamic model established in this paper, the dynamic responses of air-launch-to-orbit system during separation process are simulated with CFD/CSD/RBD coupling method and ROM/CSD/RBD coupling method, respectively. The simulation settings are as follows: Mach number is 0.7, angle of attack is 2 deg, the physical simulation time is 0.5 s. For the CFD-based simulation, the time step is 0.001 s and the surface pressure contours of the aircraft at different time are shown in Fig. 19. For the ROM-based coupling method, the governing equation is shown in Equations (26), and the physical time step is 0.0001 s. With different simulation methods, the dynamic responses of spacecraft are shown in Fig. 20 to Fig. 22.

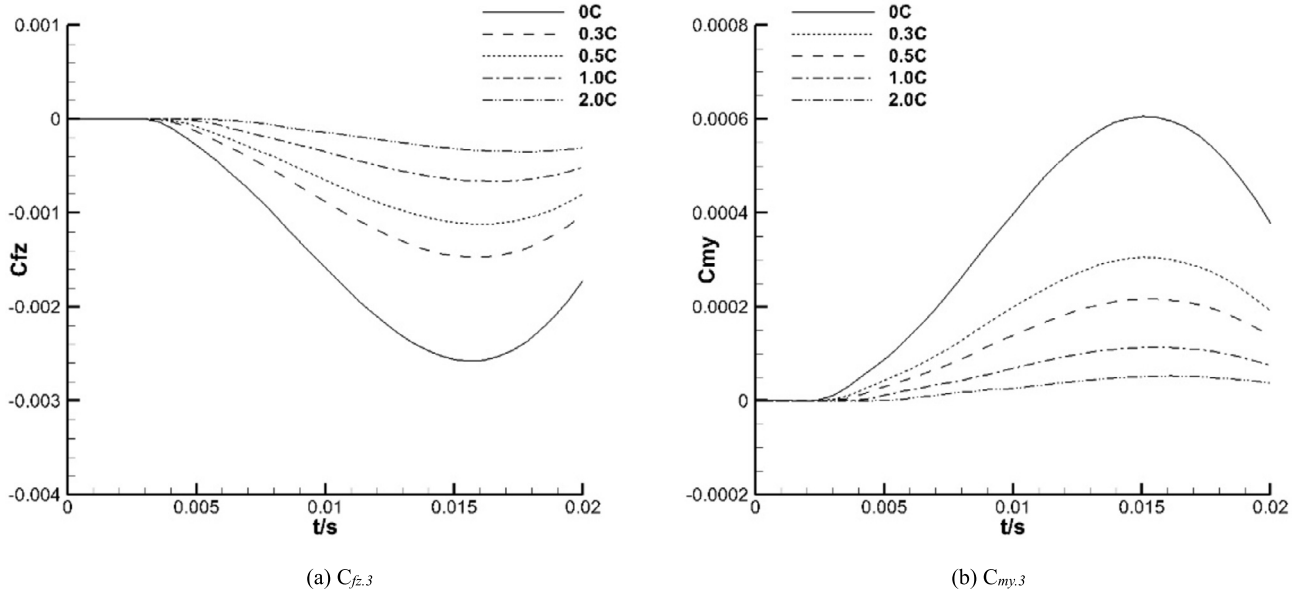


Fig. 14. The zero-mean value of the interference aerodynamic coefficients of the spacecraft.

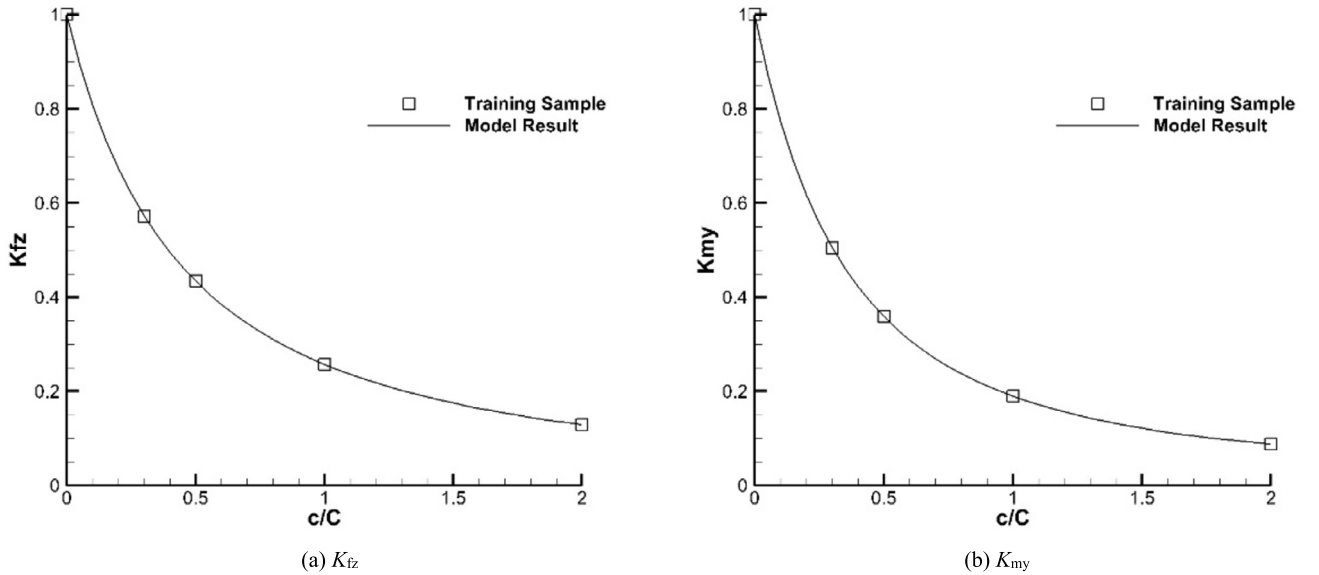


Fig. 15. Comparison between model results and training samples.

Fig. 20 shows the response curve of interference aerodynamic scale factor  $K$ . As we can see,  $K$  decrease as the simulation progresses, and the interference aerodynamic increment of spacecraft decrease. At 0.5 s, the scale factor of normal force and pitching moment are 0.0569 and 0.1438, respectively. The spacecraft is almost out of the aerodynamic interference zone of the carrier.

In Fig. 21, after separation, the relative distance between the two vehicles gradually increases, and the pitch angle of spacecraft exhibits slowly convergence and highly oscillatory. The frequency of the pitch angle curve is about 4.45 Hz, which is much lower than the first order mode of carrier. There is no modal coupling between the two vehicles. By comparison, the trends of normal displacement and pitch angle responses of spacecraft with ROM-based method and CFD-based method are the same. As shown in Fig. 23, through Fourier analysis, the frequency of the pitch angle responses with two different simulation methods are identical. However, at about 0.46 s, the peak value of the pitch angle results of ROM-based method is bigger than that of CFD-based method. The half-life period difference of pitch angle responses between the two methods is about 0.14 s. At this time, as the spacecraft is about to leave the aerodynamic interference zone of the carrier, the error does not have an essential effect on dynamic stability of spacecraft.

Fig. 22 show the comparison of the generalized displacement of carrier between ROM/CSD/RBD results and CFD/CSD/RBD results. For the first two order modes, the frequency, amplitude and mean value of curves that are predicted by ROM-based method agree well with that of CFD-based method. For the third and fourth order modes, the frequency and amplitude results of the two method are almost the same, the mean values are different. As the absolute values of generalized displacement of the two modes are relatively small, and the error of mean value is in the order of  $10^{-6}$ , which is acceptable. To sum up, the aerodynamic modeling method developed in this paper has a certain precision and can predict the dynamic response trends of the system accurately.



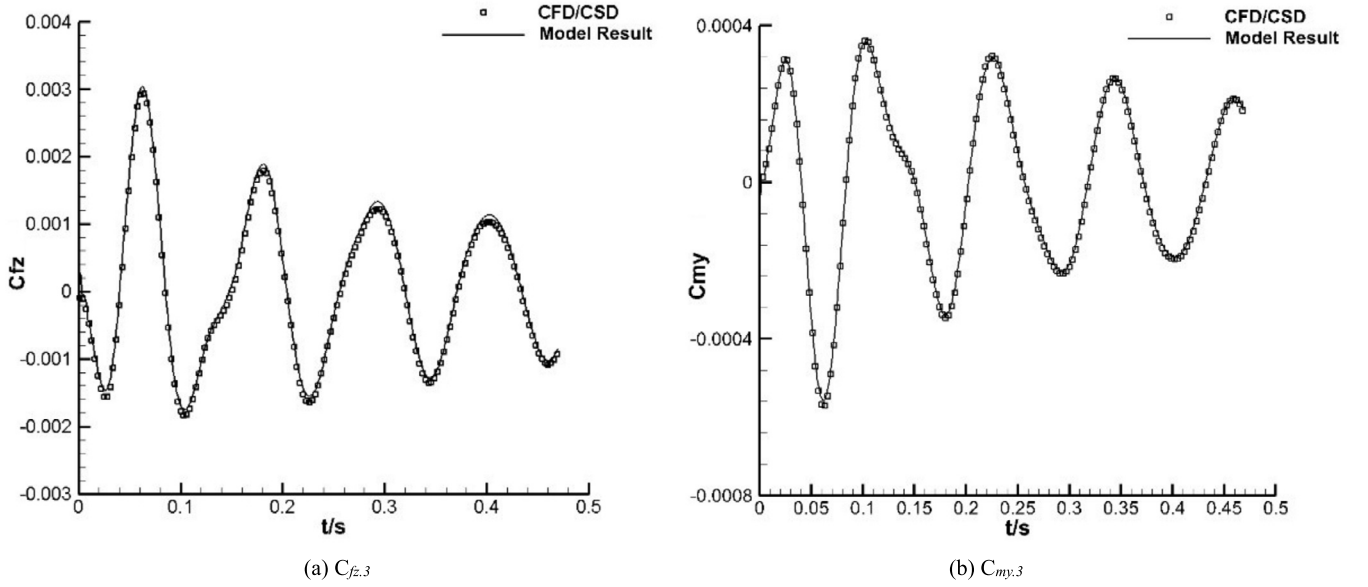


Fig. 16. Comparison between models and CFD/CSD results when the relative distance is 0.3C.

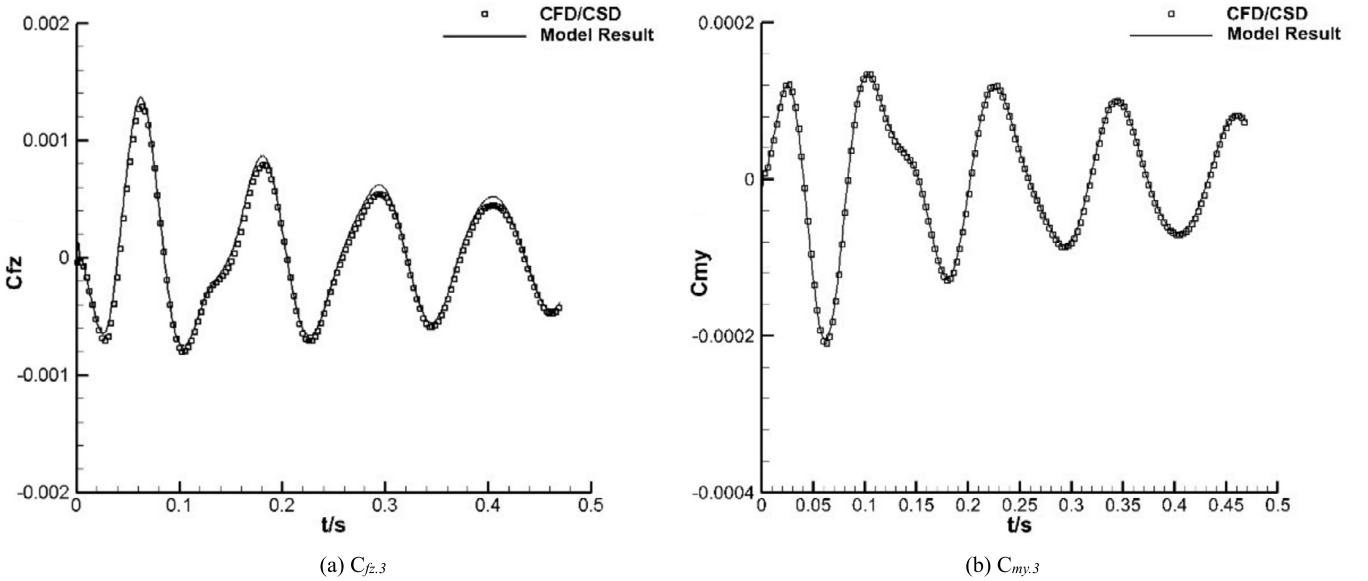


Fig. 17. Comparison between models and CFD/CSD results when the relative distance is 0.5C.

## 5.2. Error analysis of baseline case

As mentioned above, for the simulation results of dynamic response of spacecraft, there are errors between ROM/CSD/RBD and CFD/CSD/RBD methods. In this section, the reason of those errors is analyzed.

In dynamic modeling process, based on the fourth physical assumption of this paper, the interference aerodynamics of the carrier caused by the spacecraft is ignored. This is the main reason for the dynamic response error between different calculation methods. The verification is as follows.

Taking the results of generalized displacement curves of carrier with CFD/CSD/RBD calculation method as input parameters, the separation process of spacecraft is simulated with ROM/CSD/RBD method. The difference between the simulation in this section and section 5.1 is that the generalized displacement responses of carrier include the influence of spacecraft on it. The simulation results are shown in Fig. 24 and agree well with CFD/CSD/RBD results. This shows that when considering the impact of spacecraft on the carrier, the error will be eliminated to the greatest extent.

In the process of aerodynamic modeling, if the impact of spacecraft on the carrier is considered, the accuracy of the solution can be improved. However, the input parameters dimensions of the carrier aerodynamic model will be greatly increased, and the number of training samples and calculated amount will increase exponentially.

Therefore, in order to balance calculation accuracy and modeling efficiency, it is necessary to grasp the main contradictions and appropriately ignore the secondary contradictions.

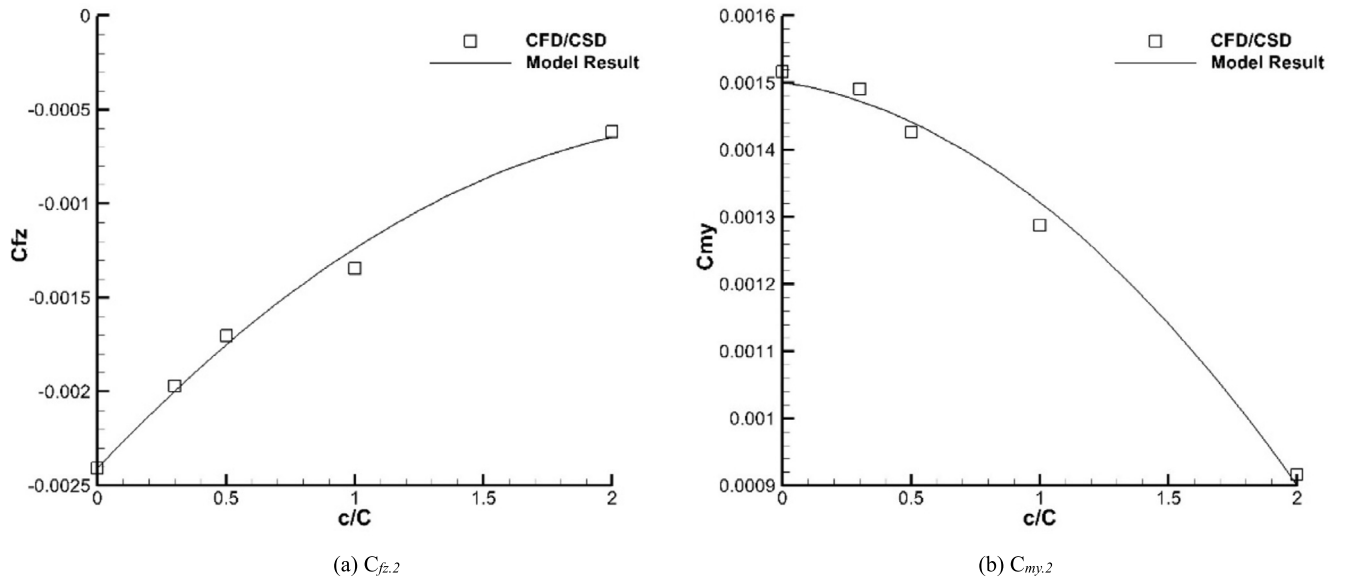


Fig. 18. Comparison between models  $C_{f,2}$  and CFD/CSD results.

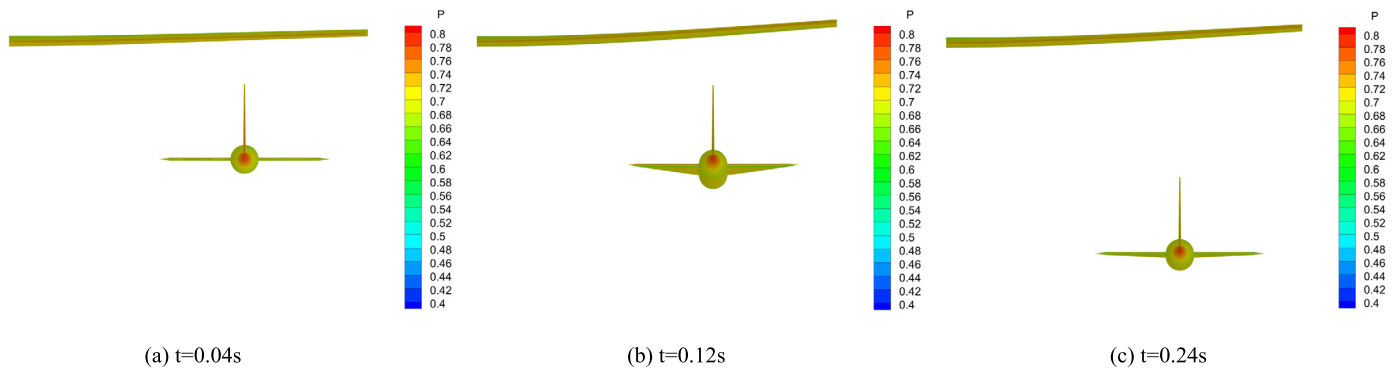


Fig. 19. The surface pressure contours of the aircrafts at different times. (For interpretation of the colors in the figure(s), the reader is referred to the web version of this article.)

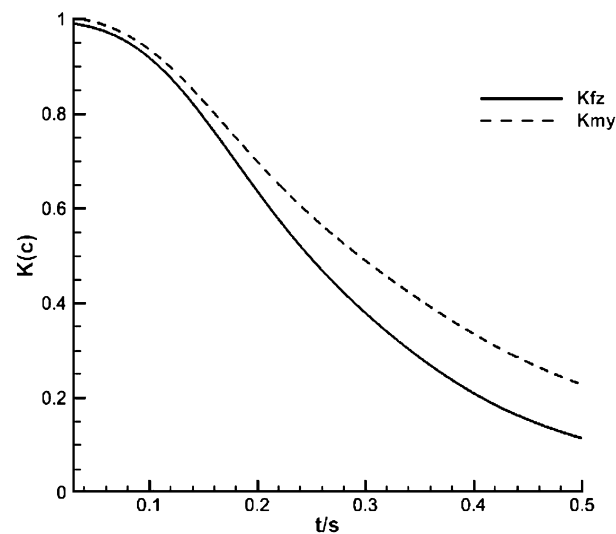


Fig. 20. Response curve of interference aerodynamic scale factor  $K$ .

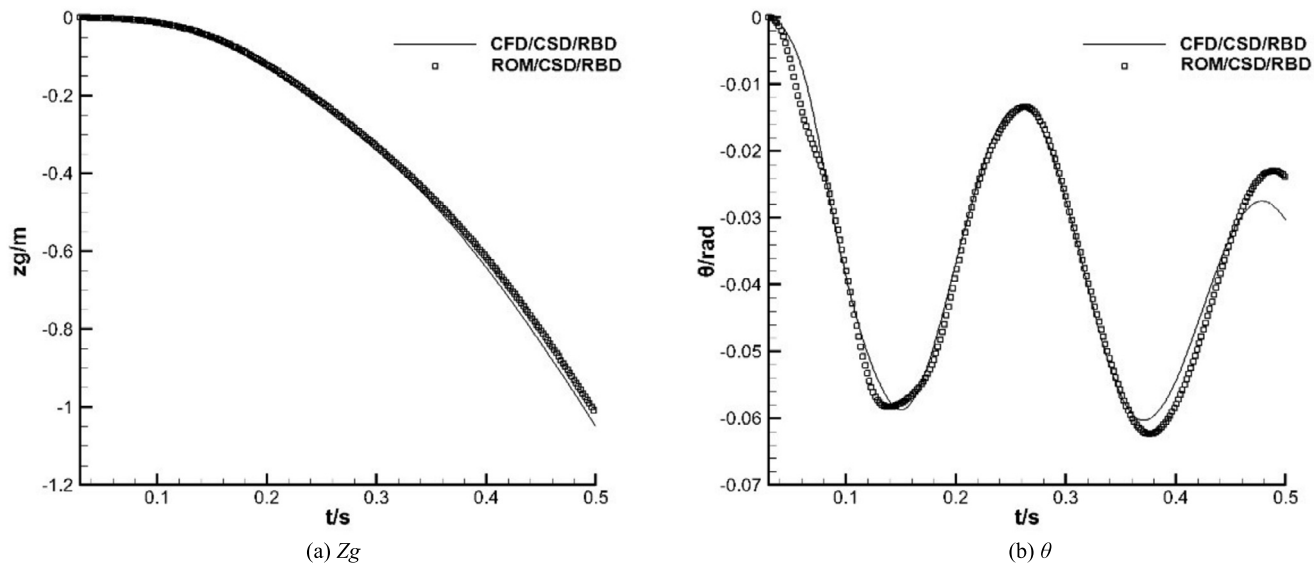


Fig. 21. Comparison of the dynamic response of spacecraft between ROM/CSD/RBD results and CFD/CSD/RBD results.

Table 6

The CUP time of the training samples.

Training sample	CPU time
Aerodynamic model of carrier	64 h
Aerodynamic model of spacecraft	96 h
Interference aerodynamic model of spacecraft	36 h
Total time	196 h

Table 7

The CUP time of dynamic simulation.

Physical simulation time	0.5 s	1.0 s	2.0 s
ROM/CSD/RBD method	196 h	196 h	196 h
CFD/CSD/RBD method	960 h	1920 h	3840 h

### 5.3. Other validation cases

In order to verify the simulation method in this paper further, more validation cases are carried out. On the basis of the baseline case, additional case 1 increases the initial installation angle of spacecraft from 0 degrees to 5 degrees (0.08727 rad) and additional case 2 reduces the dynamic pressure to one-half. The simulation results are shown in Fig. 25 and Fig. 26. By comparison, the normal displacement and pitch angle responses of spacecraft with ROM-based method agree well with CFD-based results.

### 5.4. Computational cost analysis

The CPU times of the training samples of ROM are shown in Table 6. For carrier, the aerodynamic modeling requires about 64 hours of CPU time. And for the spacecraft, the total CPU time is about 132 hours. Once the model is established, it is applicable to all working conditions included in the sample domain, and the simulation cost can be ignored. Thus, for the ROM-based simulation method, the total CPU time is about 196 hours. However, for the CFD-based method, the calculated amount is proportional to the physical simulation time, and it is about 1920 h/s (as shown in Table 7). Thus, when the total physical simulation time is  $n$  second, the CPU time of CFD-based method is  $9.8n$  times that of ROM-based method. And when the physical simulation time is above 1.02 s, the CPU time of ROM-based method can reduce by one order of magnitude comparing with CFD-based method.

## 6. Conclusion

In this study, a new reduced-order modeling method is developed, which is for unsteady aerodynamics of the air-launch-to-orbit system with considering the elastic deformations of carrier. Based on the physical mechanism of interference aerodynamics factors, the model input parameters are decoupled and the modeling difficulty is reduced. By coupling the unsteady aerodynamic model, structural dynamics equations and rigid body dynamic equations, the longitudinal dynamic responses of air-launch-to-orbit system during stage separation are simulated. According to the results, some conclusions are obtained as follows:

1. The new reduced-order modeling method is suitable for the unsteady aerodynamics of air-launch-to-orbit system during stage separation, and it has a certain precision and can predict the dynamic response trends of the system accurately.

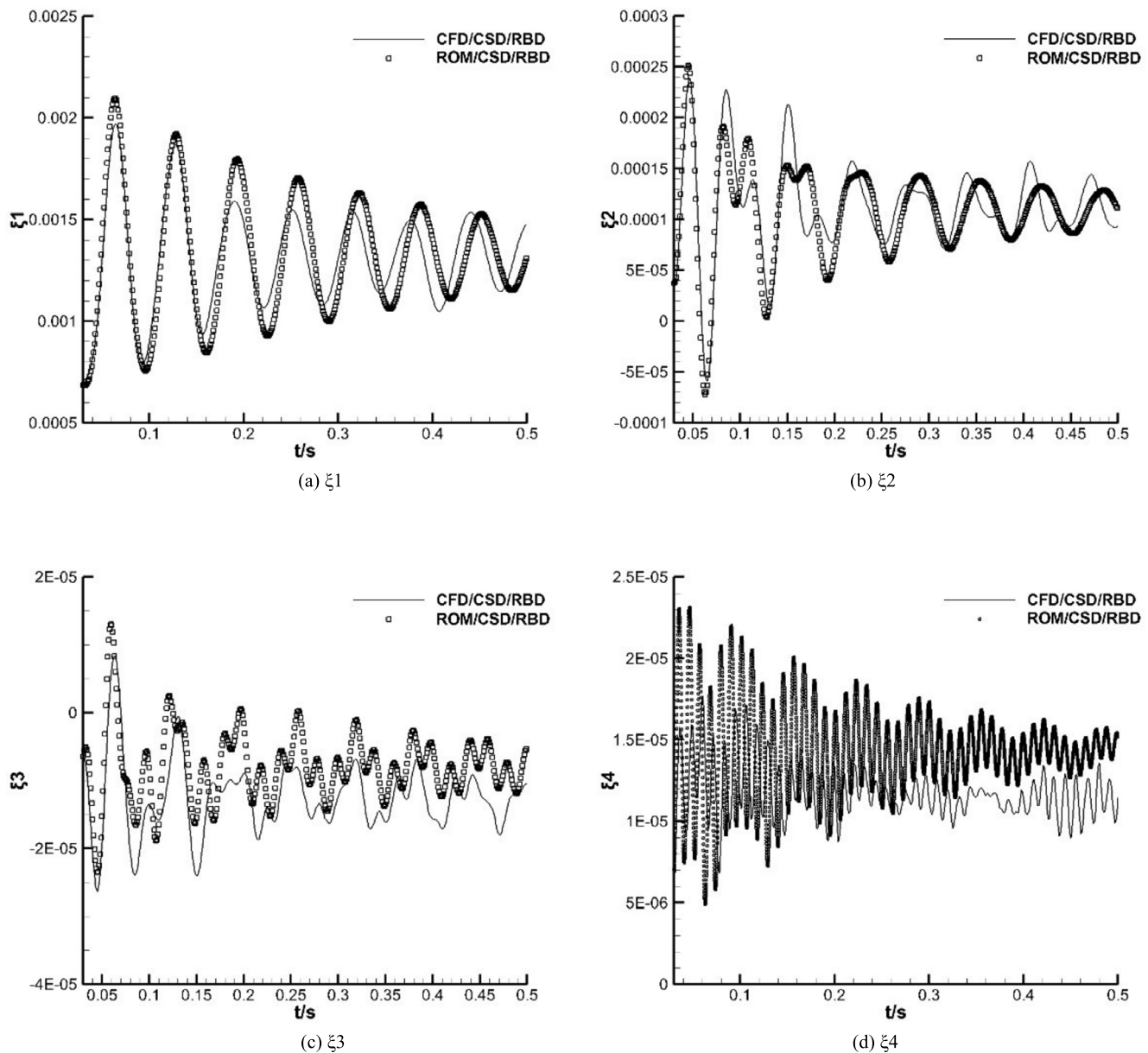


Fig. 22. Comparison of the dynamic response of carrier between ROM/CSD/RBD results and CFD/CSD/RBD results.

2. The total CPU time of ROM-based simulation method is reduced a lot compared with CFD-based method. When the physical time of time-domain simulation is greater than 1.02 s, the calculation amount can reduce by more than an order of magnitude. This method has high efficiency and can be applied to similar engineering problems.

### Declaration of competing interest

The authors declare that they have no known competing financial interests or personal relationships that could have appeared to influence the work reported in this paper.

### Acknowledgements

This work is supported by the Strategic Priority Research Program of Chinese Academy of Sciences (Grant No. XDA17030100).

### References

- [1] S.M. Poth, M.A. Fisher, D.W. Levy, et al., Design of an airborne launch vehicle and an air launched space booster, Paper AIAA 1993-3955.
- [2] F.R. Amer, L.S. He, K. Ali, et al., Multidisciplinary design of air launched satellite launch vehicle: performance comparison of heuristic optimization methods, *Acta Astronaut.* 67 (2010) 826–844, <https://doi.org/10.1016/j.actaastro.2010.05.016>.
- [3] S. Henri, P.L. Helene, J.L. Farges, Analysis and optimization of an air-launch-to-orbit separation, *Acta Astronaut.* 108 (2015) 18–29, <https://doi.org/10.1016/j.actaastro.2014.11.043>.
- [4] S.K. Marti, S.K. Nesrin, M. Bob, et al., Flight testing of a new Earth-to-orbit air-launch method, *J. Aircr.* 43 (2006) 577–583, <https://doi.org/10.2514/1.18559>.

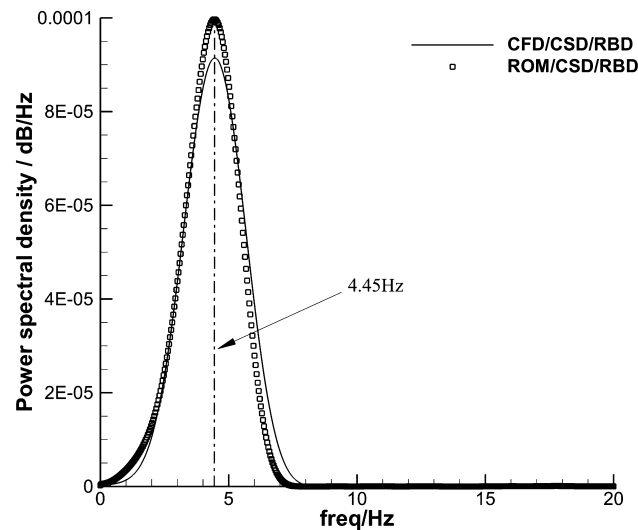


Fig. 23. Power spectral density of pitch angle response of spacecraft.

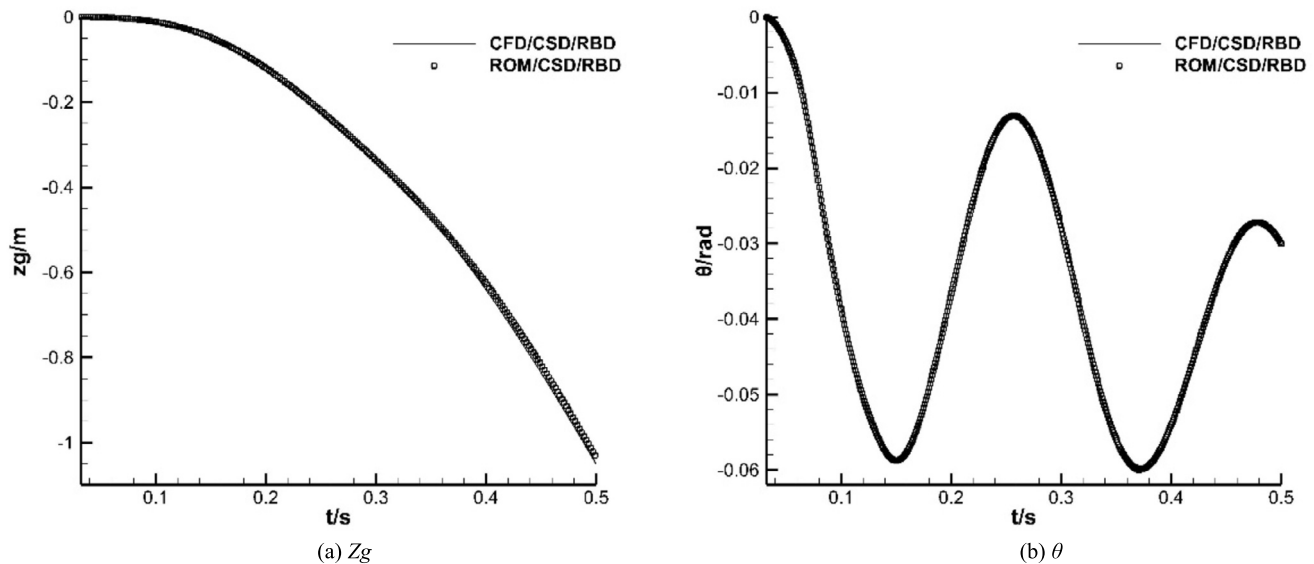


Fig. 24. Comparison of the dynamic response of spacecraft between ROM/CSD/RBD results and CFD/CSD/RBD results.

- [5] S.K. Marti, S.K. Nesrin, G.C. Hudson, et al., Gravity air launching of Earth-to-orbit space vehicles, Paper AIAA 2006-7256.
- [6] C.A. Maddock, L. Ricciardi, M. West, Conceptual design analysis for a two-stage-to-orbit semi-reusable launch system for small satellites, *Acta Astronaut.* 152 (2018) 782–792, <https://doi.org/10.1016/j.actaastro.2018.08.021>.
- [7] L. Yang, Z.Y. Ye, J. Wu, The influence of the elastic vibration of the carrier to the aerodynamics of the external store in air-launch-to-orbit process, *Acta Astronaut.* 128 (2016) 440–454, <https://doi.org/10.1016/j.actaastro.2016.07.029>.
- [8] L. Yang, Z.Y. Ye, The interference aerodynamics caused by the wing elasticity during store separation, *Acta Astronaut.* 121 (2016) 116–129, <https://doi.org/10.1016/j.actaastro.2015.12.039>.
- [9] W. Song, B.C. Ai, X.J. Zhao, et al., Influence of control device on store separation from an open cavity, *Aerosp. Sci. Technol.* 106 (2020) 1–11, <https://doi.org/10.1016/j.ast.2020.106117>.
- [10] F. Xue, Y.C. Wang, H. Qin, Derivation and validation of wind tunnel free-flight similarity law for store separation from aircraft, *Aerosp. Sci. Technol.* 97 (2020) 1–9, <https://doi.org/10.1016/j.ast.2019.105614>.
- [11] E. Heim, *CFD wing/pylon/finned-store mutual interference wind tunnel experiment*, AEDC-TSR-91-P4, 1991.
- [12] L. Lijewski, N. Suhs, Chimera-eagle store separation, Paper AIAA 1992-4569.
- [13] J.U. Ahmad, S.P. Shanks, P.G. Buning, Aerodynamics of powered missile separation from F/A-18 aircraft, AIAA 1993-0766.
- [14] C. Baird, E. Koper, *Seek eagle F-15E mixed loads certification, 975521, U.S. Air Force, 1997*.
- [15] J.M. Lee, K.S. Dunworth, M. Rizk, et al., Studies of combined use of CFD and wind tunnel test approaches to simulate a store separation from F-15E using efficient CFD database generation, AIAA 2004-4724.
- [16] R.C. Snyder, W.E. Roberts, Application of platform knowledge and adaptation of store separation analysis and testing to multiple-carriage weapon suspension systems: a case study, in *F-16/BRU-57*, AIAA 2006-454.
- [17] M. Rizk, B. Jolly, Aerodynamic simulation of bodies with moving components using CFD overset grid methods, AIAA2006-1252.
- [18] X.T. Li, Y.L. Lang, J.Q. Kou, et al., Reduced-order thrust modeling for an efficiently flapping airfoil using system identification method, *J. Fluids Struct.* 69 (2016) 137–153, <https://doi.org/10.1016/j.jfluidstructs.2016.12.005>.
- [19] G. Chen, D.F. Li, Q. Zhou, et al., Efficient aeroelastic reduced order model with global structural modifications, *Aerosp. Sci. Technol.* 76 (2018) 1–13, <https://doi.org/10.1016/j.ast.2018.01.023>.
- [20] D.F. Li, A.D. Ronch, G. Chen, et al., Aeroelastic global structural optimization using an efficient CFD-based reduced order model, *Aerosp. Sci. Technol.* 94 (2019) 1–13, <https://doi.org/10.1016/j.ast.2019.105354>.

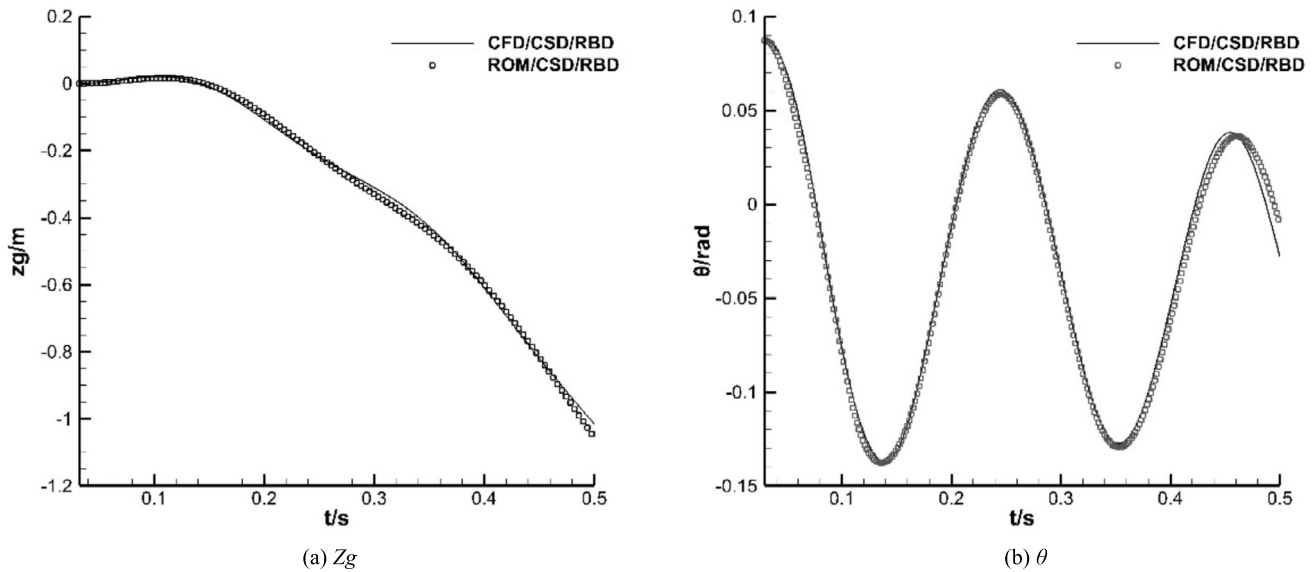


Fig. 25. Comparison of the dynamic response of spacecraft between ROM/CSD/RBD results and CFD/CSD/RBD results (Initial installation angle of spacecraft is 0.08727 rad).

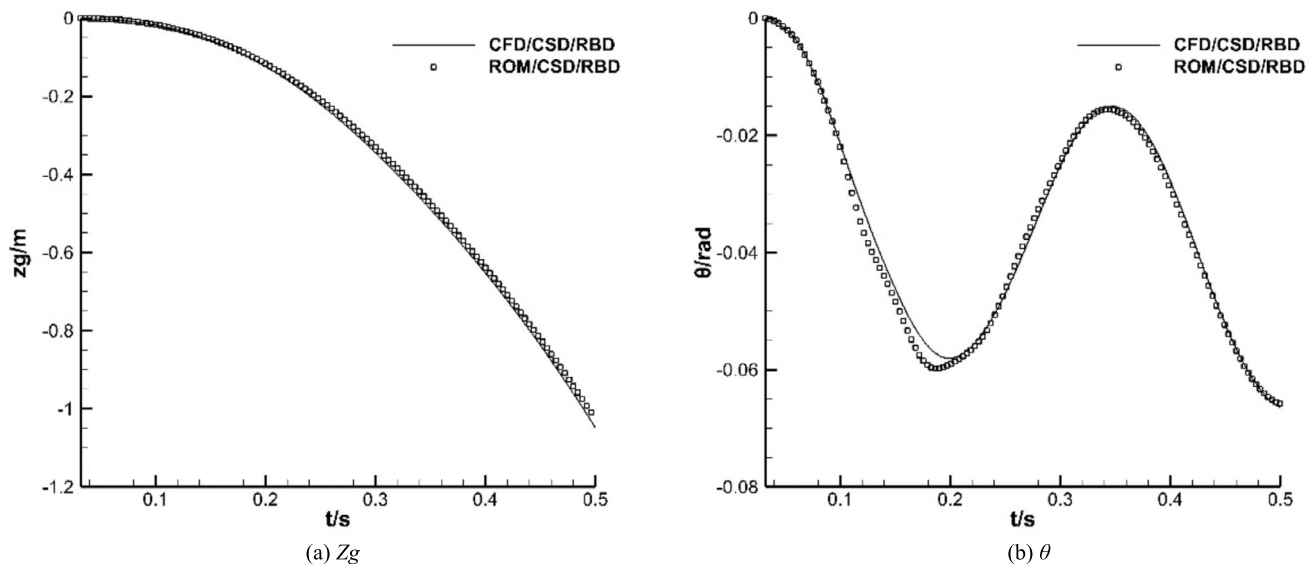


Fig. 26. Comparison of the dynamic response of spacecraft between ROM/CSD/RBD results and CFD/CSD/RBD results (Dynamic pressure is half of the baseline case).

- [21] L. Shi, H.W. Ma, X.H. Yu, POD analysis of the unsteady behavior of blade wake under the influence of laminar separation vortex shedding in a compressor cascade, *Aerosp. Sci. Technol.* 105 (2020) 1–15, <https://doi.org/10.1016/j.ast.2020.106056>.
- [22] A.L. Kaminsky, K. Ekici, Reduced-order model-based convergence acceleration of reverse mode discrete adjoint solvers, *Aerosp. Sci. Technol.* 93 (2020) 1–16, <https://doi.org/10.1016/j.ast.2019.105334>.
- [23] W.G. Yao, S. Marques, T. Robinson, et al., A reduced-order model for gradient-based aerodynamic shape optimization, *Aerosp. Sci. Technol.* 106 (2020) 1–11, <https://doi.org/10.1016/j.ast.2020.106120>.
- [24] L.L. Zhou, L.J. Jiu, Z. Jun, et al., Aerodynamic shape optimization by continually moving ROM, *Aerosp. Sci. Technol.* 99 (2020) 1–20, <https://doi.org/10.1016/j.ast.2020.105729>.
- [25] C. Yang, K. Liang, Y.F. Rong, et al., A hybrid reduced-order modeling technique for nonlinear structural dynamic simulation, *Aerosp. Sci. Technol.* 84 (2019) 1–10, <https://doi.org/10.1016/j.ast.2018.11.008>.
- [26] W.W. Zhang, Z.Y. Ye, Effect of control surface on airfoil flutter in transonic flow, *Acta Astronaut.* 66 (2009) 999–1007, <https://doi.org/10.1016/j.actaastro.2009.09.016>.
- [27] D. Huang, *Unsteady Aerodynamic Characteristics for the Aircraft Oscillation in Large Amplitude*, Nanjing University of Aeronautics and Astronautics, 2007.
- [28] E.C. Yates, AGARD standard aeroelastic configurations for dynamic response I-Wing 445.6, AGARD Report No. 765, 1988.
- [29] Y.W. Jiang, *Numerical Solution of Navier-Stokes Equations on Generalized Mesh and Its Applications*, Northwestern Polytechnical University, 2013.
- [30] Y.W. Jiang, Algebraic-volume meshfree method for application in finite volume solver, *Comput. Methods Appl. Mech. Eng.* 355 (2019) 44–66, <https://doi.org/10.1016/j.cma.2019.05.048>.
- [31] Y.W. Jiang, General mesh method: a unified numerical scheme, *Comput. Methods Appl. Mech. Eng.* 369 (2020) 1–28, <https://doi.org/10.1016/j.cma.2020.113049>.
- [32] R.H. Hua, C.X. Zhao, Z.Y. Ye, et al., Effect of elastic deformation on the trajectory of aerial separation, *Aerosp. Sci. Technol.* 45 (2015) 128–139, <https://doi.org/10.1016/j.ast.2015.04.015>.
- [33] R.H. Hua, Z.Y. Ye, J. Wu, Effect of elastic deformation on flight dynamics of projectiles with large slenderness ratio, *Aerosp. Sci. Technol.* 71 (2017) 347–359, <https://doi.org/10.1016/j.ast.2017.09.029>.
- [34] H. Li, Z.Y. Ye, Numerical investigation on aerodynamic and inertial couplings of flexible spinning missile with large slenderness ratio, *Aerosp. Sci. Technol.* 99 (2020) 1–14, <https://doi.org/10.1016/j.ast.2019.105582>.



- [35] K. Ye, Z.Y. Ye, C.N. Li, et al., Effects of the aerothermoelastic deformation on the performance of the three-dimensional hypersonic inlet, *Aerosp. Sci. Technol.* 84 (2019) 747–762, <https://doi.org/10.1016/j.ast.2018.11.015>.
- [36] L. Yang, Q.H. Sun, A multi-time scale solution strategy for an elastomeric aircraft, *Aerosp. Sci. Technol.* 103 (2020) 1–13, <https://doi.org/10.1016/j.ast.2020.105884>.